PARTIALLY PREMIXED TUBULAR FLAMES:

AN EXPERIMENTAL SURVEY

By

Darren C. Tinker

Thesis

Submitted to the Faculty of the

Graduate School of Vanderbilt University

In partial fulfillment of the requirements

For the degree of

MASTER OF SCIENCE

in

Mechanical Engineering

December, 2016

Nashville, Tennessee

Approved:

Robert W. Pitz, Ph.D.

Amrutur V. Anilkumar, Ph.D.

Haoxiang Luo, Ph.D.

DEDICATION

For Sheba. Your aggressive nuzzling and enthusiastic greetings will be missed.

ACKNOWLEDGEMENTS

I thank my adviser, Dr. Robert W. Pitz, for his guidance and support. His encouragement has allowed my exploration of a new area in tubular flames and provided opportunity to develop skillsets for my career as a researcher. I thank him for his patience, as both my mentor and as my instructor, which created an environment for me to freely interact with colleagues who share my career path and goals. He succeeds in being not only an advisor, but also a mentor and friend.

I thank Carl A. Hall for his aid during my experimental and numerical research campaigns. Gratitude extends also to my lab-mates Chad Carpenter, Will Bearden, and Dexter Watkins. Words do not suffice.

I also send my thanks to Jason and Jennifer Dooley and Sarah DeGeorge for their endless support in reviewing my work and providing encouragement.

Support for this work and my efforts has been provided by the National Science Foundation under Grant CBET-1606005 and through Vanderbilt's Mechanical Engineering Department. Thank you.

Finally, I thank my friends and family for their support and faith throughout my endeavors. My parents had a hell of a time instilling the work-ethic and values that I have today, and I am grateful for it all. I hope their part in my successes is never overlooked.

TABLE OF CONTENTS

Page

LIST OF TABLES

LIST OF FIGURES

NOMENCLATURE

A	Area
Fr	Froude number
H	Outer nozzle exit height
Le	Lewis number
PPTF	Partial premixed tubular flame
R	Nozzle diameter
V	Nozzle velocity
W	Axial velocity gradient
d	Characteristic length
g	Gravity constant
k	Stretch rate
r	Radial coordinate
t	Time
u	Velocity
x	Mole fraction
z	Axial coordinate

Greek Letters

α	Thermal diffusivity
D	Molecular diffusivity
ϕ	Equivalence ratio
ρ	Density
τ	Timescale

Subscripts

r	Radial coordinate
st	Stoichiometric conditions
z	Axial coordinate
1	Inner nozzle
2	Outer nozzle

CHAPTER 1:

INTRODUCTION

1.1. BACKGROUND

The ultimate goal for combustion science is to efficiently and accurately simulate turbulent combustion. With this computational ability, design of combustors used in heating, energy production, transportation, and defense needs will be optimized to produce reliable, compact, and robust combustion devices that are safer and economical. However, this goal is at least a generation away due to current computational resources and accuracy of underlying assumptions in existing turbulent models.

Before high accuracy turbulent simulations become a reality, the field must tackle less complex problems where parameters of combusting flows can be isolated. Laminar flames are computationally inexpensive to model and simulate in full detail, thus permitting efficient evaluation and comparison of different chemical mechanisms and transport phenomena. It is by understanding fundamental aspects of combustion that the field will improve the quality of existing turbulent models. In turn, the study of canonical laminar flames is a necessary and paramount stepping stone to true comprehension of combustion phenomena.

Regardless whether studying turbulent or laminar flames, specificity in the type of combustion is a requirement. Flames with the oxidizer and fuel combined before reacting are deemed premixed, whereas flames requiring the oxidizer and fuel to mix during the reaction are aptly named diffusion flames. Pure premixed and pure diffusion flames dictate the extremities of the combustion spectrum, with most real-world flames occurring somewhere in between. That regime of combusting flows is known as partially premixed combustion and is prevalent across a myriad of combustors: stove-tops, water-heaters, jet-engines, power-generation, etc. Due to their pervasiveness in modern devices and the desire to expand upon a strong foundation of knowledge, characterization is needed from both numerical and experimental standpoints.

Experimentation leads to many difficulties, especially when battling the four-dimensional challenge known as combustion. Reactions, heat loss and gain, diffusion, and advection fluctuate across spatial and temporal scales. Simplification is key. Varieties of burners have been developed to produce steady-state laminar flows, eliminating fluctuation with time but still maintaining spatial complexity. Creation of planar flames by axial-opposed jets reduces the problem to two dimensions, but the flames are planar, unlike practical flames that are usually curved. The design and implementation of the tubular burner, with radially-opposed jets, at Vanderbilt has allowed the benefits of reduced spatial dimensions as seen in axial-opposed jet flames, and offers the ability to isolate the parameters of stretch rate and curvature from each other.

Opposed jet flames and tubular flames are similar with respect to flow stagnation, but generate unique flame structures. Reactants for an opposed jet enter along the axial coordinate, stagnate, and exit along the radial direction. Tubular burners act in the opposite manner, entering radially, stagnating and then exiting along the axial dimension. A simplified schematic in Figure 1 depicts differences between the two flows. The change from two opposed planes to an opposed annular flow of reactants geometrically alters the flame structure. The opposed jet produces a thin sheet along a plane parallel to the jets, and the tubular burner produces a flame in the shape of a tube, axial-symmetric about the same axis as the burner nozzle.

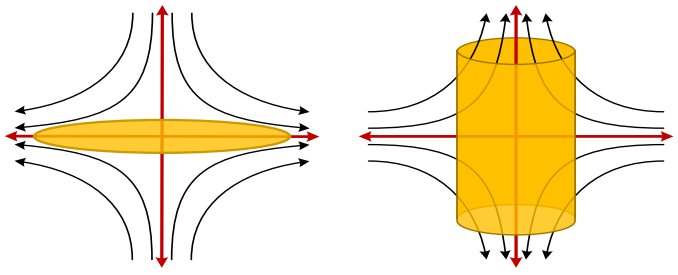

Axial Opposed Jet Flame

Radial Opposed Jet Flame
(Tubular Flame)

Figure 1 - Schematic of opposed jet flames and tubular flames. Each are stagnating flows with stagnation about the radial and axial coordinate respectively.

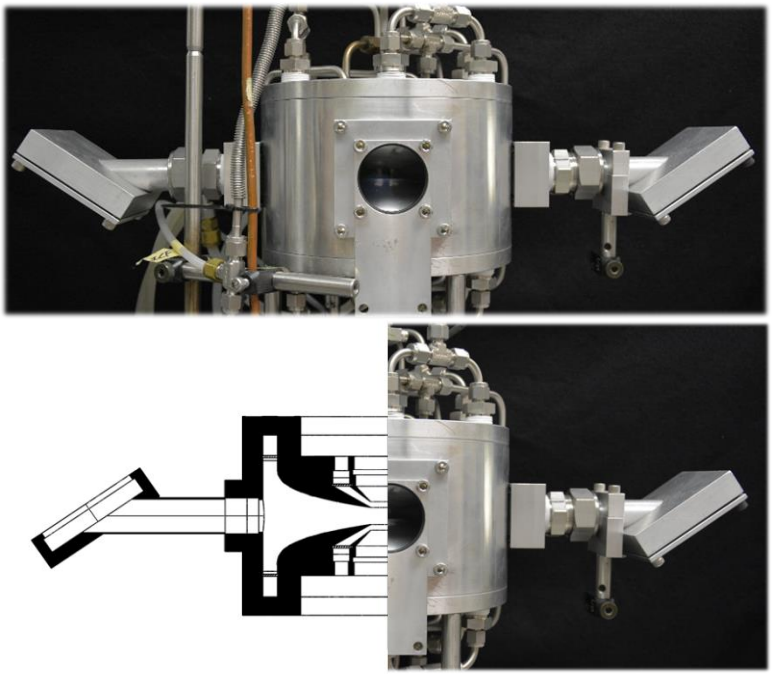

Figure 2 - Vanderbilt's tubular burner as seen in lab (above), and with a mirrored schematic juxtaposed (below)

Researchers at Vanderbilt have redesigned and manufactured a tubular burner [1], verifying laminar-flow as well as uniform plug-flow velocity from the outer nozzle. The burner itself, juxtaposed with a CAD cutout, can be seen in Figure 2. The reacting flow domain is a 24 mm diameter with an 8 mm nozzle height with non-reacting co-flow nozzles to preserve uniform inlet velocities and temperature. Optical access for laser diagnostics is permitted by two opposed windows at Brewster angles and a window perpendicular to both the laser line of sight and exhaust gases. Optical access above and below the burner, in-line with exhausts, is available by line-of-sight or reflected images. The tubular flame is mounted vertically along the axis of the burner to avoid buoyancy effects seen elsewhere [2]. Without modification, as seen in Figure 3 (left), the burner is capable of creating premixed flames with all reactants exiting the outer nozzle. Addition of a porous pipe, an inner nozzle, modifies the flow domain and permits formation of tubular diffusion flames with the oxidizer exiting the outer nozzle and fuel exiting the inner nozzle as seen in Figure 3. The inner nozzle is 6.2 mm in diameter and has an 8 mm section in height for fuel with the remainder of the nozzle designed as a co-flow. For partially

premixed flames, lean premixed gases are introduced by the outer annular nozzle and diluted fuels exit the porous inner nozzle. A detailed schematic of the burner is found in Figure 4, showing how partially premixed flames are created.

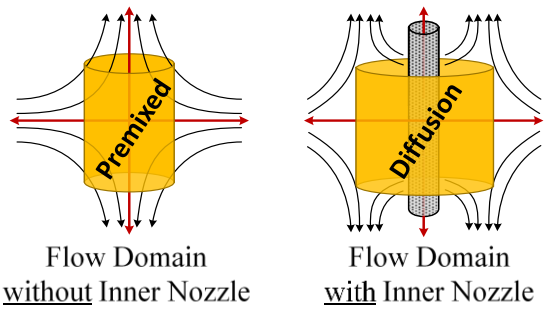

Figure 3 - Differences between premixed (left) and diffusion (right) tubular flame domains. Diffusion flames are generally larger due to addition of the inner nozzle and have a cylindrical stagnation surface as opposed to a stagnation line in the flow field

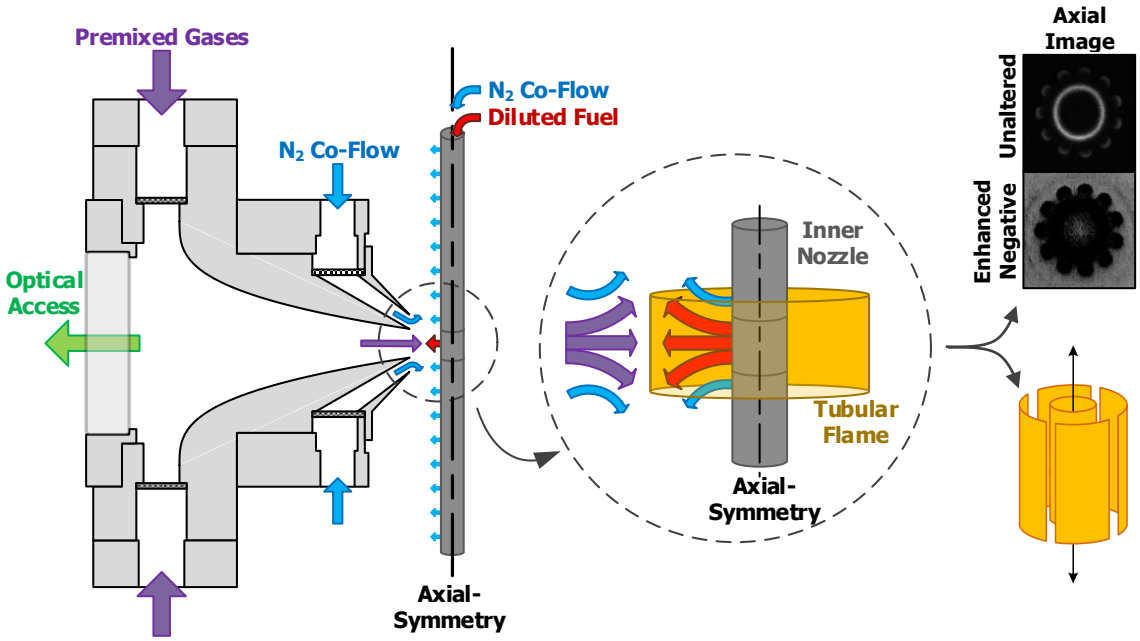

Figure 4 - Detailed schematic of tubular burner cutout. Premixed reactants enter the outer nozzle and are opposed by diluted fuel from the inner nozzle. Axial images and a flame schematic are on the right to depict size relative to the outer nozzle and flame structure.

1.2. INSTABILITIES

Real world combustion devices are prone to instabilities that can have devastating effects on both rocket and gas turbine combustion systems [3, 4]. Large-scale instabilities may derive from the entire system containing the combustor or possibly from the combustor geometry alone, and control systems are developed to mitigate the dangers of high-pressure combustion instabilities [4]. Small-scale instabilities are unlikely to be regulated by adaptive design processes and result from the fundamental characteristics of the combustion process. Small-scale effects are known as intrinsic instabilities and are the foundation for beautiful and complex behaviors where flame surfaces wrinkle, fold, oscillate, and break into cells [5]. Cellular flames have local extinction zones which is a prevalent and intricate phenomenon. Both hydrodynamic and thermal-diffusive instabilities are shown as a cause for cellular formation [5], but in tubular flames [6, 7], most instabilities are caused by the thermal diffusive effect.

Thermal-diffusive instabilities are explicitly dominant in flames with Lewis numbers (Le) deviating from unity. The Lewis number (Le) is the ratio of thermal diffusion (α) over molecular diffusion (*D*). For partially premixed flames, two Lewis numbers exist, one for the premixed reactants and the other for the diffusion gases and take the form shown in Equations 1,

$$Le = \frac{\alpha}{D} = \frac{Thermal\ Diffusivity}{Molecular\ Diffusivity} \tag{1}$$

where α is the mixture averaged thermal diffusivity and D is the molecular diffusivity. For a two-component mixture D and α can be determined from equations 2 and 3 as found in transport phenomena theory [8].

$$\alpha = \frac{\mathrm{k}}{\rho * \mathrm{c_p}} \tag{2}$$

$$D = \frac{1.858 * 10^{-3} * \mathrm{T}^{3/2} * \left(\frac{1}{\mathrm{M_1}} + \frac{1}{\mathrm{M_2}}\right)^{0.5}}{\mathrm{p} * (0.5 * (\sigma_1 + \sigma_2))^2 * \Omega} \tag{3}$$

Where k is the thermal conductivity, ρ is the fluid density, c_p is the specific heat, T is the temperature, M_1 and M_2 are the molar masses, p is the pressure, σ_1 and σ_2 are the collisional diameters, and Ω is the temperature-dependent collision integral. In premixed flames, the molecular diffusivity is for the deficient reactant within the bulk mixture, which is the fuel for lean flames and the oxidizer for rich flames. For nonpremixed flames, the molecular diffusivity will depend on the gas stream, creating two Lewis numbers, one for the molecular diffusivity of the fuel and one for the molecular diffusivity of oxidizer. Figure 5 represents calculations of the Lewis number for partially premixed flames in this work. The bulk mixture properties following the premixed flame is calculated as if complete combustion occurred.

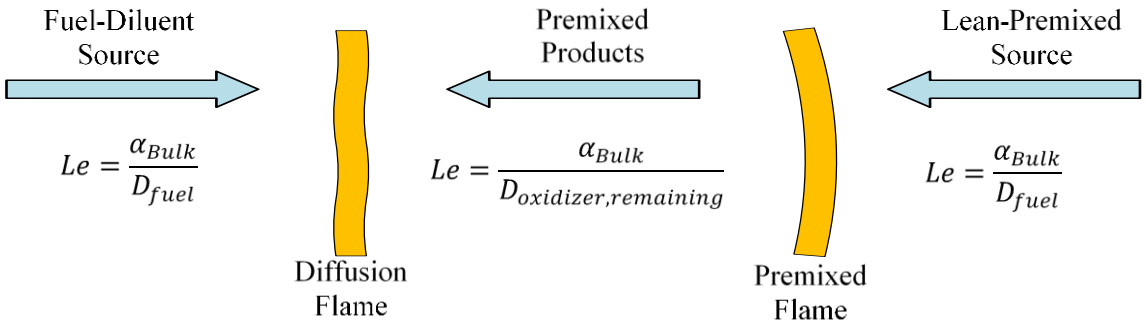

Figure 5 - Lewis number definitions for a partially premixed tubular flame. Bulk mixtures are determined for each zone based on species present. The premixed products zone assumes complete reaction from the premixed flame when calculating α_{Bulk}.

Previous investigations for premixed tubular flames have shown that equidiffusive (Le = 1) premixed methane-air flames do not form cells, leading to the understanding that thermal-diffusive effects are the leading cause of cellular instability [9]. For Lewis number values less than unity, thermal transport phenomena are overpowered by molecular diffusion, and lead to the creation of cellular flames. Sub-unity Le tubular premixed flames have been studied thoroughly in the past and produced a significant amount of cellular flame cases for experimental campaigns with laser diagnostics [9]. Low Le flames benefit from convex curvature toward the fuel source [10], and high Le flames burn stronger from the inverse behavior. Super-unity Lewis number

tubular flames have not been studied as extensively [2], and a brief examination occurs here for partially premixed tubular flames.

1.3. TUBULAR FLAMES

Tubular burners have been predominately involved in studies of premixed flames and diffusion flames with low Lewis numbers. These flames have characteristics of turbulent flames, - local extinction zones, varying curvature, and zones of enhancement, - yet exist in a laminar and steady state flow that offers considerable advantages for diagnostic techniques. For the burner at Vanderbilt, diffusion flames are created using the geometry shown previously in Figure 4 with the oxidizer exiting the outer nozzle and fuels exiting a porous pipe that acts as the inner nozzle. Diffusion flames have cellular modes near extinction and mostly exhibit a concave curvature toward the incoming fuel flow. Premixed flames are created solely with the outer nozzle and are convex in nature toward the fuel.

Tubular flame profiles are diverse and range from non-cellular rings or tubes, to distinct and symmetric cells. These flames are primarily characterized by their stretch rates, initial mixture strength, and equivalence ratio due to the variety of flame behaviors by altering these parameters. The equivalence ratio (Equation 4) and initial mixture strength (Equation 5) take nearly identical forms, yet are only valid for premixed and diffusion flames respectively.

$$\phi = \frac{x_f}{x_o} \Big/ \left(\frac{x_f}{x_o}\right)_{st} \tag{4}$$

$$\varphi = \frac{x_f}{x_o} \Big/ \left(\frac{x_f}{x_o}\right)_{st} \tag{5}$$

In both equations, x is the gas mole fraction, subscript *st* denotes stoichiometric conditions, and subscripts *f* and *o* represent the fuel and oxidizer. The equivalence ratio (ϕ) is the simplest, using mole fractions from the premixed gas stream. Since diffusion flames consist of two reactant sources by definition, they cannot be characterized by the equivalence ratio. Thus, for the initial

mixture strength (φ), x_f and x_o represent the mole fraction in the fuel-stream and the oxidizer stream respectively. Note, the equivalence ratio (ϕ) as used in this work references the premixed gases exiting the outer nozzle and has no bearing on the output of the inner nozzle. For the equivalence ratio (ϕ), values less than one are considered lean combustion, and values greater than one represent rich combustion. Lean reactions are environmentally preferred due to their clean burning nature, but are difficult to maintain due to instabilities in combustors which leads, once more, to the need to understand cellular instability in laminar flames.

Cellular behavior is impacted considerably by varying stretch rates. Stretch rate is the expansion or contraction of the reacting zone and is known as a primary cause of flame extinction [11]. The simplest analysis considers the reaction zone to be infinitely thin relative to the normal direction of flow. The flame structure is then simplified to a two-dimensional plane allowing stretch rate to be evaluated as,

$$k = \frac{1}{A}\frac{dA}{dt} \tag{2}$$

where A is the flame surface area. Analytic solutions to cold-flow stretch rates in tubular flames have been derived in prior work [12], which also produced solutions for the stagnation radius, an analogous property to the stagnation plane in opposed jet burners. For the tubular burner with an inner nozzle, the resulting equations for stretch and the stagnation radius are,

$$k = \pi\frac{V_1}{R_1}\left(\frac{\frac{V_2R_2}{V_1R_1}\sqrt{\frac{\rho_2}{\rho_1}}-1}{\left(\frac{R_2}{R_1}\right)^2-1}\right) \tag{6}$$

$$R_s = R_2\sqrt{1-\frac{\frac{R_2}{R_1}-\frac{R_1}{R_2}}{\frac{R_2}{R_1}-\frac{V_1}{V_2}\sqrt{\frac{\rho_1}{\rho_2}}}} \tag{7}$$

where subscripts 1 and 2 represent the inner and outer nozzles respectively, and velocities are relative in direction. Results to follow in this work were calculated at the room conditions: 298 K and 760 torr.

The appreciation for past work on partially premixed flames cannot be overlooked. Past work has comprised multiple flame structures under the title partially premixed such as double, triple (tribrachial), and edge flames; understanding of extinction of partially premixed flames is important for fire suppression and characterization [13]. Other studies have illustrated that partially premixed flames become more resistant to strain extinction due to increased interaction from concentration gradients, the existence of optimum levels of inhomogeneity in inlet mixtures with regards to flame stability, and the boost to flame speed within back-supported flames [14]. Opposed flow burners and specially designed burners have been used to create triple flames that consist of rich and lean flames surrounding an inner diffusion flame; these studies have provided stability maps and shown the effects of stretch rates on flame behavior [15]. As with premixed and jet diffusion flames, the effects of curvature are difficult to isolate with these burners and warrant investigation with tubular flames.

For this work, a variety of partially premixed flames have been studied using both experimental and numerical methods for multiple fuels and burner inlet conditions. Partially premixed tubular flames (PPTF) are created using both inner and outer nozzles, as are used when making pure diffusion flames. Fuel and diluent exit the inner nozzle, meeting an oxidizer stream from the outer nozzle. With no premixing of the oxidizer stream, a partially premixed flame begins as a diffusion flame. Fuel is then added to the oxidizer stream and eventually forms a flame with qualities resembling both premixed and diffusion flames studied in the past. The hybrid response has never been seen before in experimental work with tubular burners and offers a plethora of data to study. The different types of flames are schematically shown in Figure 6.

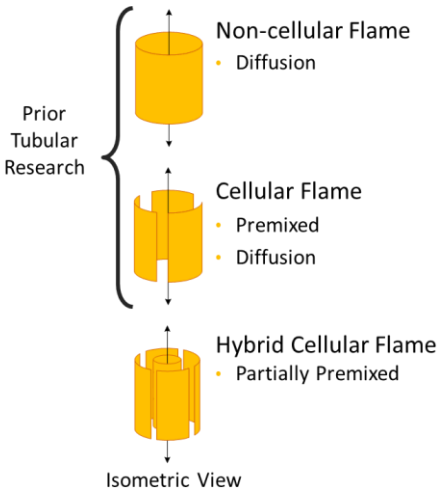

Figure 6 - Schematics of non-cellular, cellular, and hybrid cellular tubular flames with respective reactant mixtures to create each flame

Past experimental work on tubular flames has consisted of chemiluminescence imaging, Raman Spectroscopy, and laser induced fluorescence (LIF) for hydroxyl and atomic hydrogen measurements. Recent work on tubular flames has involved development of an in-house code to simulate tubular flames in full detail [6]. This code has been largely validated against premixed and diffusion flame data. Application and validation of the code for partially premixed flames is the next logical phase. Numerical work in tubular flames has been studied by multiple groups [16, 17, 18, 19] and the information gathered through this experimental campaign is to serve as a qualitative benchmark for future simulation results of partially premixed flames. In short, due to the novelty of partially premixed tubular flames, the objectives of the research are: 1) parametrically survey and analyze stable flame geometry via chemiluminescence and 2) perform Raman spectroscopy on select cases to develop a fundamental understanding of flame composition as a foundation for numerical comparison and validation.

CHAPTER 2:

A SURVEY OF PARTIALLY PREMIXED FLAMES

2.1. PARTIALLY PREMIXED TUBULAR FLAME CHARACTERISTICS

Under the current burner geometry and parametric sweeps, partially premixed tubular flames (PPTFs) form a variety of shapes. Those particularly of interest contain clearly defined premixed and diffusion zones from chemiluminescence imaging, seen respectively as cellular and non-cellular modes. Near conditions conducive to flashback (where the flame enters the outer nozzle and extinguishes), the cells change shape and form a split cell, reasonably named due to its appearance in pairs. Differences between the reaction types and examples of cells are found in Figure 7, and an artistic rendering of the flame structure is shown in Figure 8 for clarity. Past tubular flame cases contained only cellular or non-cellular flames in premixed or diffusion modes, which have been investigated thoroughly. The existence of both modes in a single instance offers a higher level of complexity where one can examine interactions between diffusion and premixed flames.

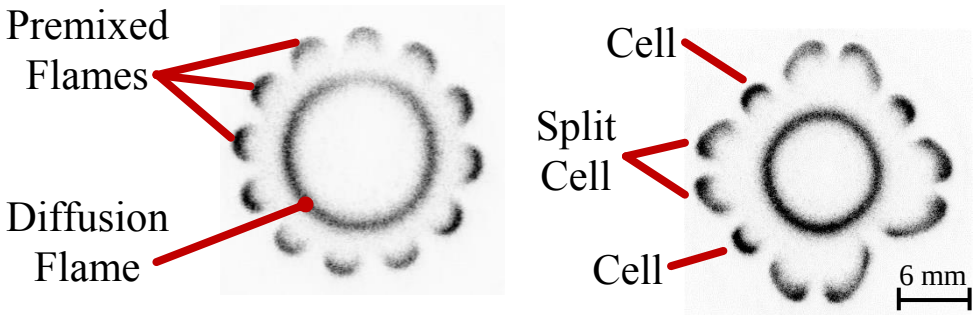

Figure 7 - Left: A steady-state PPTF showing characteristics of both a non-cellular diffusion flame and premixed cellular flames. Right: A steady-state PPTF containing premixed cellular flames (singular cells) as observed in past tubular work and groups of novel split cells

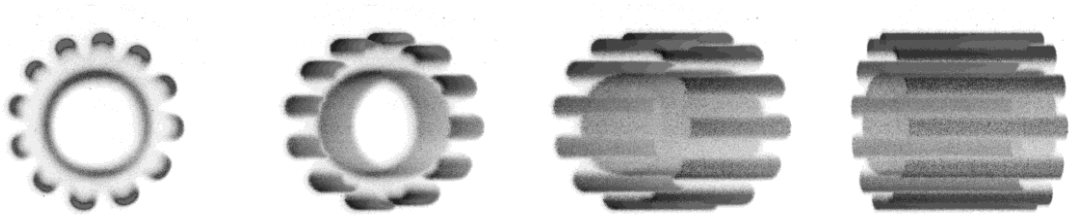

Figure 8 - Artistic rendering of a PPTF rotated perpendicular to the axis of symmetry to depict a tubular flame in three dimensions. Flames retain good symmetry along the axial direction near the measurement area.

2.2. FROUDE NUMBER

Low values of stretch rate produce flames lacking axial-symmetry. The non-uniform rings are intuitively understood as the impact of buoyant forces on the flame as the hot product exits the burner axially. The Froude number is largely depicted as the ratio of convective to buoyant forces, and its inverse has been used when analyzing laminar diffusion flames [11]. Adaptation to a timescale reference has been used in the past to analyze tubular flames [1], producing the equations (8 - 10)

$$\tau_{fl} = \frac{R_2 - R_1}{V_f + V_o} \tag{8}$$

$$\tau_{by} = \sqrt{d/g} \tag{9}$$

$$Fr = \frac{Covective\ time\ scale}{Buoyant\ time\ scale} = \left(\frac{\tau_{fl}}{\tau_b}\right)^2 \tag{10}$$

where τ_{fl} and τ_{by} are the flow and buoyancy timescales, and Fr is the Froude number. For values of $Fr \gg 1$, convective forces dominate the flow, and buoyancy has negligible effects.

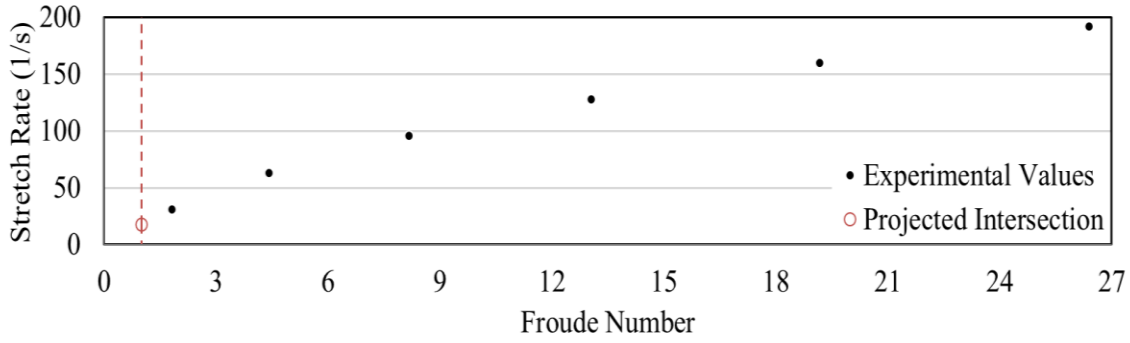

Figure 9 - Froude numbers vs. stretch rate for the primary experimental PPTF cases observed. The projected intersection of Fr = 1 for the burner geometry occurs near a stretch of 18 s^{-1}.

Both cellular and non-cellular cases with Fr ≈ 2 and k ≈ 30 s^{-1} show clear asymmetry, which is likely introduced by buoyant effects on exiting gases. Doubling the stretch rate to ≈ 60 s^{-1} and thus doubling the Froude number creates more symmetric cellular flames, but retains slight deformity in the pure non-cellular flames. At stretch rates nearing 100 s^{-1}, diffusion cells, non-cellular rings, and premixed cells all appear highly uniform and symmetric. Good symmetry is seen in flames with k ≈ 60 s^{-1} and Fr ≈ 5, and is the lowest threshold for chemiluminescent analysis. For laser diagnostics, the lowest defensible limit for measurements is with k ≈ 100 s^{-1} and Fr ≈ 8. The Reynolds number (defined as $Re = u_r * H/\nu$) at this stretch rate (100 s^{-1}) is 180, which is well below analytic values for turbulent conditions with ν approximated as 0.16 cm^2/s for air at 300 K, H as the height of the outer nozzle exit (8 mm), and an outer nozzle velocity (u_r) of 36 cm/s. The highest Reynolds number for this work is 400 when the stretch rate approaches 200 s^{-1} and is well below turbulent conditions.

2.3. PPTF Flame Variation by Premixing

Partially premixed tubular flames here are created by imposing a lean premixed gas onto a diluted fuel stream. The experiments described here have premixed gases consisting of lean hydrogen-air mixtures flowing toward hydrogen diluted with carbon dioxide. The combination of gases is chosen to produce low Lewis number mixtures and increase effects of preferential diffusion. Premixed gases exit the outer nozzle and meet the diluted fuel stream from a porous

inner nozzle. The greatest distinctions in flame response were found by varying levels of premixing during the primary investigation. Flames were found to have a variety of responses across constant stagnation radius. Chemiluminescent images were taken with a Cerco UV lens 2.8 $f/\#$ (100 mm focal length) in front of PI-Max 4 (1024 x 1024) ICCD using a UG-11 filter to capture OH* (309 nm) and broadband CO_2* with high rejection of the laser wavelength (532 nm).

For the initial survey, the stagnation radius was kept constant across corresponding stretch rates as seen in Figure 10. The structural responses were examined from the limits of flame extinction to flashback into the burner across a select range of stretch rates, shown in full detail in Figure 11. Lower limits without extinction consisted of pure diffusion flames, observed in past work [20], existing in cellular modes shaped as rounded cells and axial-symmetric cigars. Increased premixing expanded cell size to form non-cellular flames until haloes stretched out from the ring (e.g. $\phi = 0.228$, $k = 96\ s^{-1}$). Haloes were stable when near the same length scale as the diffusion flame, but became unsteady with greater premixing, and bulging and oscillating around the flame. The transitional state to form independent premixed cells predominantly formed eight premixed cells, though modes with seven and nine initial cells were observed. Higher premixing expands the radial location and sequentially the number of cells.

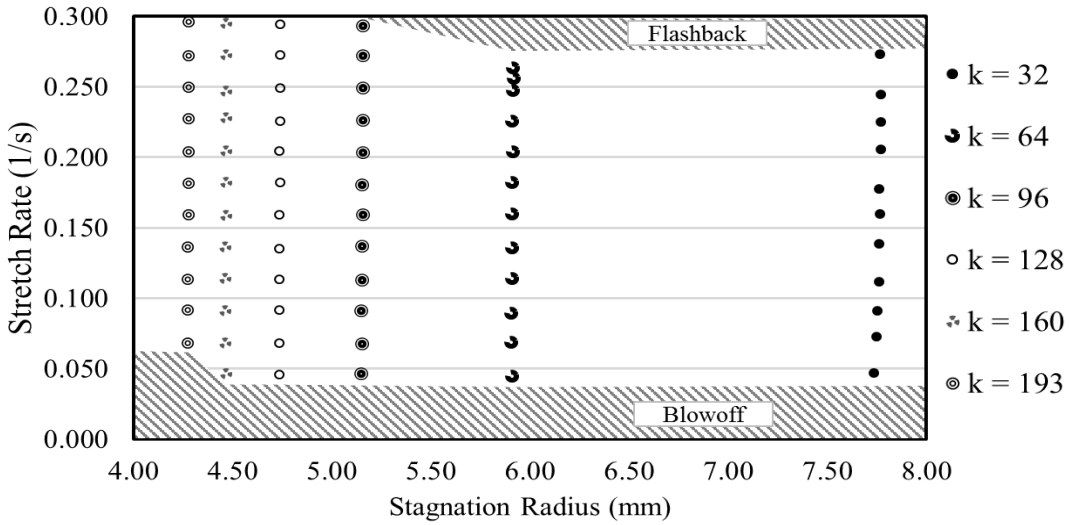

Figure 10 - Effects of stretch and equivalence ratio on stagnation radius for experimental survey of partially premixed flames, which correlate to images and conditions in Figure 11

The highest count of cells found here was thirteen, before vibrational instabilities dominated the flow. Steady state conditions return upon formation of split cells; see to Figure 7 (right) for reference. Split cells were measured with radii measuring from 10 – 11 mm for conditions here, the lower limit also being the highest measurement for singular cell radii. Axial symmetry was not necessarily present. However, images show mirror symmetry across a minimum of one plane for all stable flame cases.

Split cells are unique to PPTFs, to the author's knowledge, and the flame structures containing such cells will be referenced as "star-shaped." These cells contain regions of high and low curvature, and are ideal for numerically examining transport phenomena and further verifying effects of curvature. A second benefit is the presence of both single and split cells in a distinct flame structure. Direct comparison of single, small, highly-curved cells is possible with split cells along a range of curvatures. Chemiluminescent response alone shows greater intensity in single cells over split cells. Such a response is expected given enhancement by convex curvature toward fuel sources for similar flames. The cusped shape of split cells contains structural similarity to instabilities in laminar, planar premixed hydrogen/air flames [21], thus making tubular star-shaped flames enticing for detailed investigation with future work.

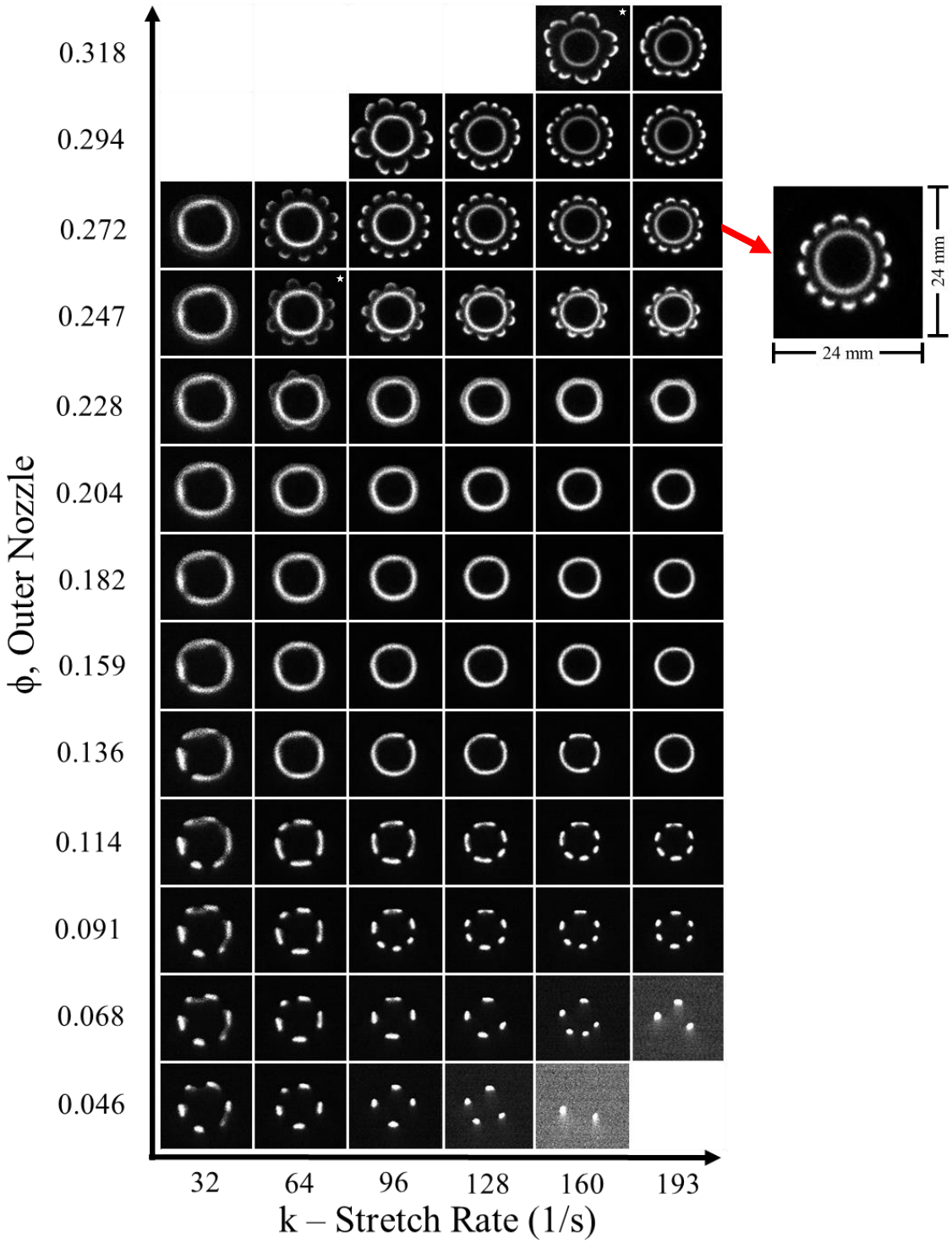

Figure 11 - Parametric map of PPTFs by varying the equivalence ratio and stretch rate at 0-90% full scale of chemiluminescence intensity. Inner nozzle dilution is constant for all cases at 14% H_2 and 86% CO_2 by mole fraction. Increased symmetry is observed with higher stretch rates for all cases. Most flames with symmetric cellular diffusion conditions are steady-state with some experiencing rotational instabilities. The majority of flames with asymmetry at higher ϕ values are transient in nature with vibrational or rotational instabilities. Non-symmetric steady state flames at high ϕ include: k = 64, ϕ = 0.247 and k = 160, ϕ = 0.318

2.4. PPTF FLAME VARIATION BY DILUTION RATES

Impacts of changing inner nozzle boundary conditions were investigated by (1) altering flow rates with constant dilution of 14% fuel by mole fraction and (2) altering dilution from 0% to nearly 50% fuel. Figure 12 shows the map of inner nozzle velocity effects, where cases were expanded from trials in the first survey across all ϕ values at a stretch of 96 s^{-1}. Inner nozzle velocities were raised and lowered by 25% of the original flowrate, maintaining the same dilution ratio. Higher flowrates, column 3, saw mild effects of jetting from the inner nozzle, causing non-uniform diffusion flames. Lower flows created tighter diffusion flames with strong consistency in the azimuthal direction. The most notable effects were observed near flashback conditions with the formation of star-shaped flames.

Tubular star-shaped flames have only been observed at large radii, requiring significant azimuthal space to form. As the premixed flame diameter increases, single cells increase in quantity, but grow unstable past certain diameters. The shift toward structures with a combination of split and singular cell flames appears as a means to stabilize the flame, likely balancing different causes of instabilities. Hydrodynamic instabilities may begin to influence flame behavior at large radii, as inferred from near unity Le premixed flames in prior work where methane-air flames form low-curvature wrinkles [22].

As constant dilution was observed to have minimal impact on most hybrid flame structures, the fuel and diluent were both cycled to determine independence of singular premixed cells and the non-cellular diffusion flame. Cycling the diluent to increase, then decrease mixture dilution, had minimal hysteresis effects on flame behavior as shown on the left in Figure 13. Only as the stagnation radius surpassed 5 mm did cells gain vibrational modes that did not lead to transitions in cell number or structure. Decreasing dilution to the original rate returned the flame to its initial state. No significant impacts on the premixed cells were observed despite irregularities in the symmetry of the diffusion flames.

Cycling the fuel had similar effects on premixed cells, no prominent impacts. As seen on the right in Figure 13, the diffusion flame remained uniform during this process and burned with greater intensity. Premixed cells, despite this, did not see variation in intensity as shown by Figure 14, even with extinction of the diffusion flame. Slight radial translation is observed in the flame structure by increase in the stagnation radius as well as greater intensity of the diffusion flame. The premixed flame behavior—when steady-state singular cells can be sustained independent of the diffusion flame—is dictated by upstream flow conditions. This behavior is similarly observed in lower hydrocarbon fuels.

At lower premixing where cells are closer to the stagnation radius, premixed cells may be greatly influenced by the diffusion flame. This comment is primarily made by observations in Figure 12 from $\phi = 0.247$, column 3. Here, premixed cells interact with the diffusion flame, forming a uniquely-structured, and steady-state flame. Numerical simulations have produced a similar flame to be discussed in a later section.

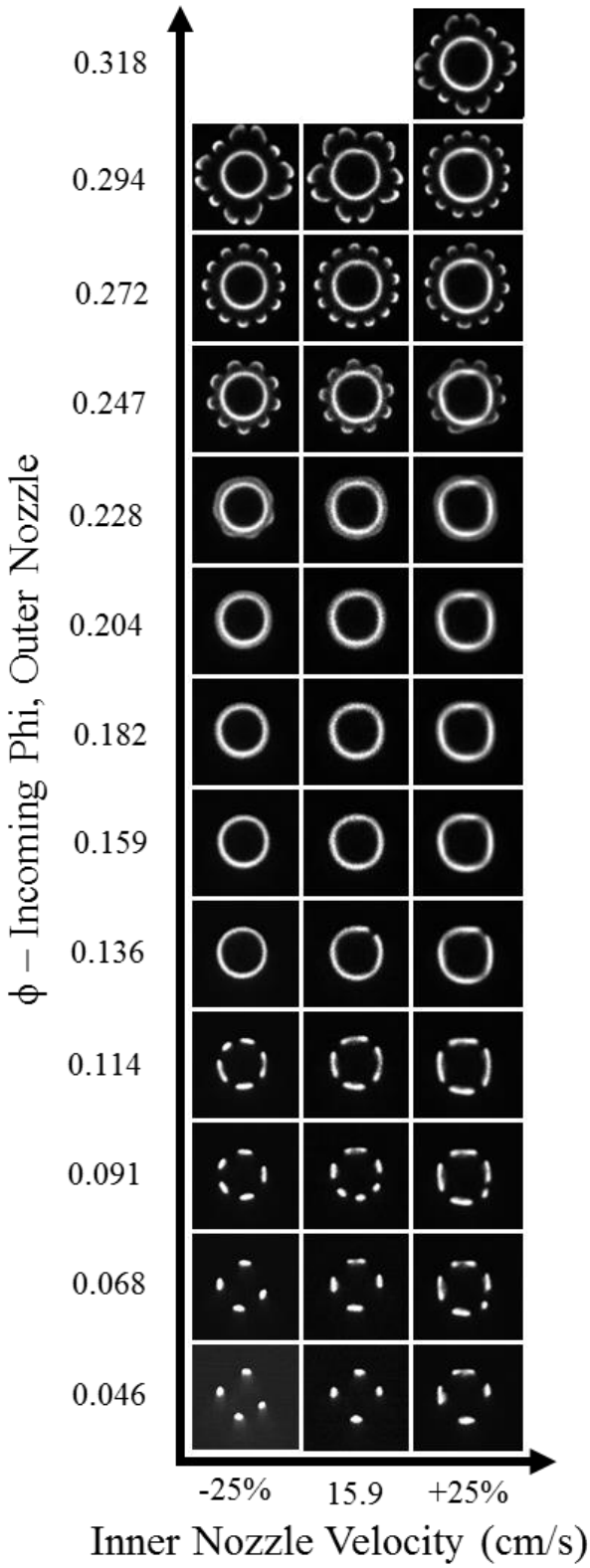

Figure 12 - Effects of varying inner nozzle velocity with constant dilution at k = 96 s^{-1} with constant inner nozzle dilution all cases at 14% H_2 and 86% CO_2 by mole fraction. The diffusion flame loses uniformity as velocities increase due to jetting from the inner nozzle.

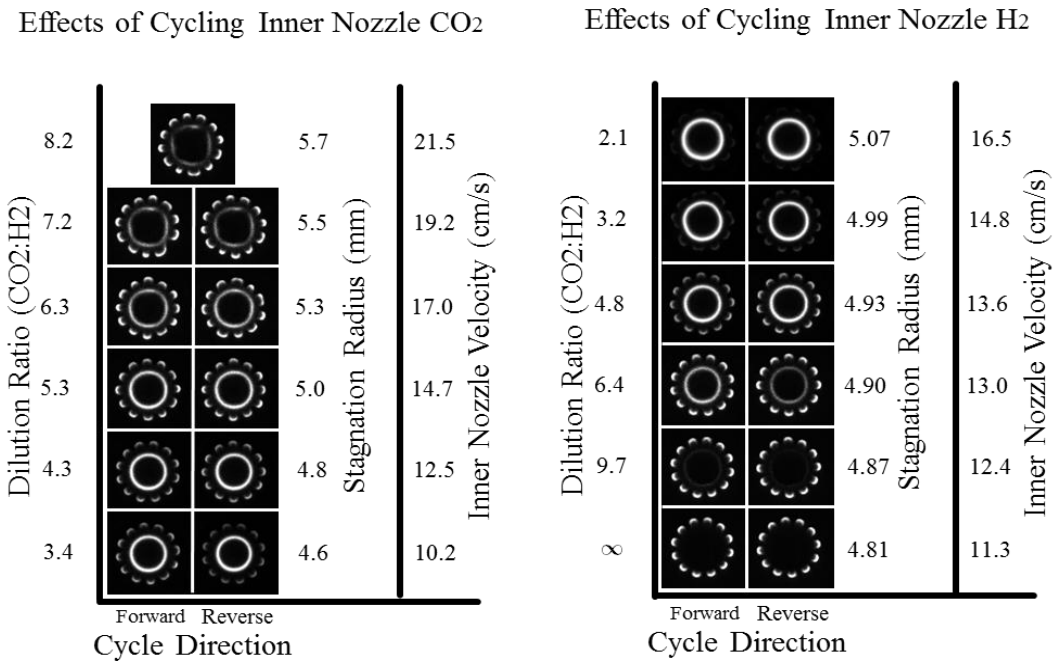

Figure 13 - Effects of cycling dilution rates at k = 90 s^{-1}, ϕ = 0.272. Premixed flame structures are largely unaffected by dilution rate or hysteresis effects. Effects of jetting from the inner nozzle are substantial for higher mass flow rates of CO_2 and interfere with premixed cell stability

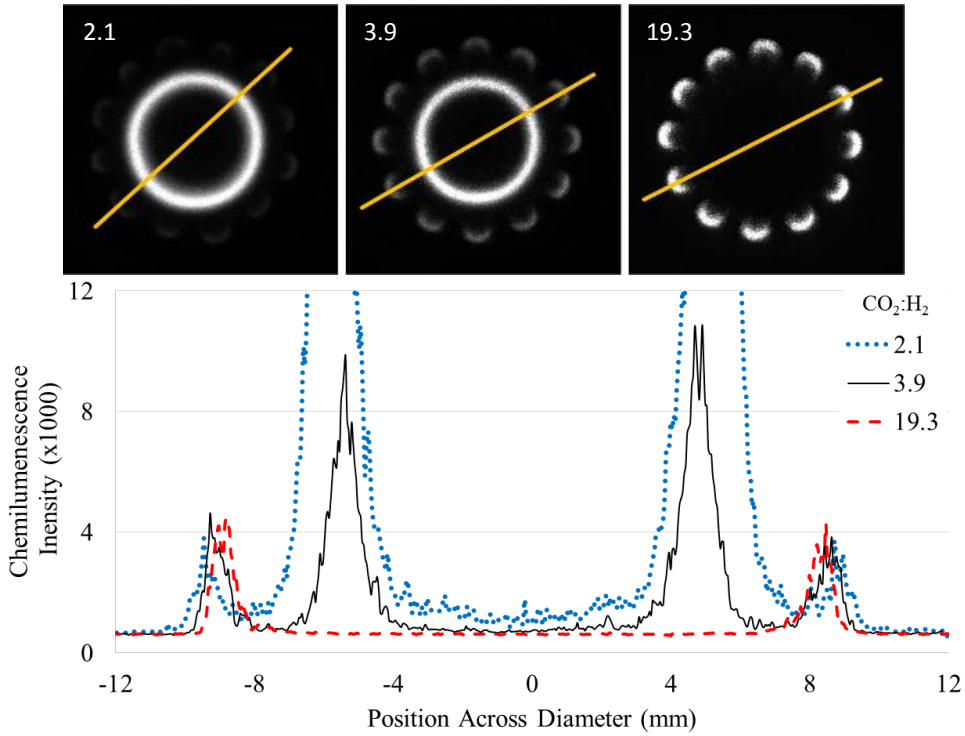

Figure 14 - 1D plot of chemiluminescent response for three dilution ratios with associated images selected from the right of Figure 13. Premixed cells see no significant change in peak intensity and are translated radially outward with higher flowrates from the inner nozzle.

2.5. METHANE AND PROPANE FLAMES

While hydrogen-air flames were the fundamental aim for this survey, a brief experimental campaign was performed with small hydrocarbon fuels. To attain both super and sub-unity Lewis number mixtures from the inner nozzle, methane and propane were used in place of hydrogen as shown in Figures 15 and 16. Images shown are scaled 0 – 97% full scale chemiluminescent intensity.

Initial trials with methane consisted of steady premixed gases (H_2-air at $\phi = 0.288$, $k = 80\ s^{-1}$) and variable dilution of methane. Pure carbon dioxide from the inner nozzle sustained 12 single cells as seen in the previous section. Initial addition of methane did not produce a non-cellular diffusion flame, but instead back-filled cells. Lower dilution (below 13% CH_4) led to both premixed and diffusion cells, unseen in hydrogen flames. The diffusion cells rapidly transitioned to an overpowering non-cellular flame, leaving the premixed cells virtually unaltered. Propane flames were considerably more sensitive to dilution rates, producing intense non-cellular flames, and were examined at 95% CO_2 dilution across select equivalence ratios for the H_2-Air mixture.

Similar to methane flames, cellular regions of diffusion flames occurred as influenced by thermodiffusive effects of hydrogen cells. As hydrogen cells expanded radially, propane diffusion cells transformed to a non-cellular ring with higher intensity behind hydrogen cells and lower intensity between cells. The most interesting behavior was the splitting of the propane diffusion flame into large concave cellular flames bounded on each end at the boundary between different sets of split cells. In contrast, the propane flame remained intact behind singular cells, though at lower intensity than when behind either side of a split cell, indicating preference for the preheated oxidizer leaving the cells. Tubular cellular flames in a mixture with Le > 1 is uncommon, but not unheard of in preceding literature, which showed preference for concavity toward the fuel source [23, 24]. As cellular flames with Le >1 have been seen in more complex flame geometries [25,

26, 27], the ability to study effects of hydrogen-propane cellularity in a simplified domain opens new potential for future experimental and numerical work.

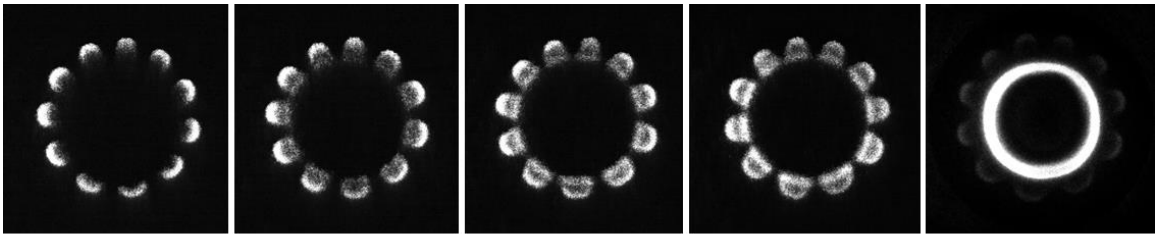

Figure 15 - Select premixed H_2-air vs. diluted methane-carbon dioxide flames at constant premixing (ϕ = 0.288, k = 80 s^{-1}). Significant back-filling of cells occurs, unlike in hydrogen-carbon dioxide dilutions, before formation of a non-cellular diffusion flame. Methane percentage from left to right is: 0, 4, 9, 13, and 17. Cellular behavior is present in 17% methane dilution and unchanged by the strong intensity diffusion flame.

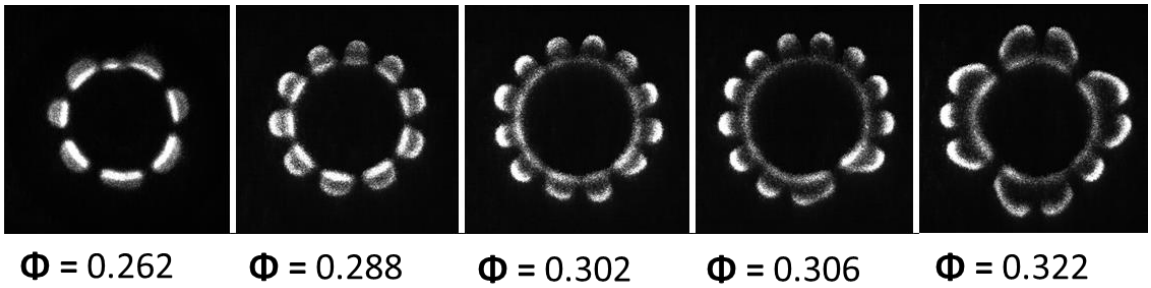

Figure 16 - A sample of premixed hydrogen-air vs. diluted propane-carbon dioxide (5% propane) flames at constant stretch of k = 90 s^{-1} at ϕ = 0.262, 0.288, 0.302, 0.306, 0.322. Attention should be given to 1) cases with both premixed and diffusion cellular flames present and 2) cases with split cells and concave diffusion flame cells

2.6. MODES OF STABLE AND UNSTABLE FLAMES

Three instability modes were observed with partially premixed tubular flames across all fuel mixtures studied here: (1) oscillatory, (2) rotational, and (3) cellular (inclusive of split cells or star-shaped flames). These instabilities are similar to those studied in counterflow flames [28] as well as premixed and diffusion tubular flames [7, 9, 18, 23].

Vibrational instabilities were observed in cells near the flashback limits and during cellular transitional states where either the number or shape of the cells varied. Examples of flames with oscillatory instabilities in Figure 11 include:

$\phi = 0.228$, k = 64, 96, 128, 160, 193 s^{-1}

$\phi = 0.294$, k = 128, 160, 193 s^{-1}

$\phi = 0.318$, k = 193 s^{-1}

Rotational modes are technically an unstable mode, yet the flame structure remained intact and constant during rotations. The revolving behavior has been largely attributed to the inner nozzle not being fully concentric with the outer nozzle. However, premixed cellular flames lacking the inner nozzle also experience rotational modes and were restrained by a wire perturbation [29]. It is subsequently expected that lack of uniformity in porosity of the inner nozzle and moderate flow rates increases cellular stability with respect to rotation.

Flower-like flame structures consisting exclusively of singular cells (resembling $\phi = 0.272$, k = 96 s^{-1}) were the most stable with regards to perturbation by wires, experiencing minor if any attraction of cells toward the wire. Flames with identical structure and with active rotation, were largely unaffected by perturbation and often continued to rotate. On removal of perturbations from the flow field, flames that had been manipulated would promptly return to their initial state. For the vast majority of symmetric cases, cells remained stationary without stabilization used previously for premixed flames [29].

Transitional states between non-cellular and cellular cases were rarely, if ever, steady-state. With increased premixing, uniform and symmetric rings grew halos that would wrinkle and oscillate along the outer edge, then transform into single cells. Growth and absorption of cells from and into a halo occurred at different premixing levels, indicating flame hysteresis as seen in premixed and diffusion cellular flames [7, 30].

Star-shaped tubular flames with split cells were highly stable from rotational modes, but not from perturbation to the flow field. Disturbances would cause structure dissipation, wild vibrations, and on occasion immediate flashback. Removal of the probe would return the flame to

its original or a similar structure. Star-shaped flames were highly dependent on behavior of the diffusion flame, in sharp contrast with singular cells that could retain their structure when the diffusion flame was fully extinguished.

CHAPTER 3:

EXPERIMENTAL AND NUMERICAL ANALYSIS

3.1. EXPERIMENTAL SETUP

Measurements of major species and temperature profiles were obtained using spontaneous Raman scattering. Linear measurements were raster scanned to form a two-dimensional planar dataset. Resolution of the measurements are 86 μm by 200 μm as verified by a Ronchi grating and set by a translation stage. The full system, sans PI-Max 4 and related chemiluminescence hardware, is shown in Figure 17. Excitation was attained by the output of a doubled Surelite Continuum III Nd:YAG (532 nm, 10 ns pulse at 10 Hz). The temporal length of the pulse was then expanded to 160 ns by passing the beam through a three-cavity pulse stretcher, cavity length ratios of 1:2:4, to reduce peak intensity [31]. Laser alignment quality was maintained by use of a burn patterns and a monochrome CCD camera as a beam monitor, sampled at the end of the pulse stretcher by a wedge window. The secondary reflection was used to measure and scale beam energy per pulse with a Molectron J25LP-3 energy meter. After passing through a periscope the beam entered a 0.3 m focal length plano-convex lens. At the point of measurement, the beam size was estimated between 175 - 200 μm with energies varying from 94 - 110 mJ per experiment.

Raman signal was collected perpendicular to the laser line using methods seen in prior work [1, 7]. Signal enters an f/2 3" diameter acromat, and is focused by a second f/7.5 3" acromat onto the slit of a modified 0.75 m Spex spectrometer (0.75 m first mirror, 0.65 m second mirror). An OG 550 filter, IR filter, optical Uniblitz shutter (model number VS25S1T0, 6 ms opening time), an OG 550 filter, an IR filter, and a ferroelectric liquid crystal (FLC) shutter (45 μs opening time) preceded the slit to create a bandpass region of 550-750 nm and reduce expose time to ≈50 μs. Incoming spectra are recorded by a liquid-nitrogen cooled charge-coupled (PI LN/CCD) camera [32]. A total of 600 shots were accumulated and integrated to produce a single image. Signal was converted to number density of major species using the equation below,

$$S_i = E \sum_j K_{ij} N_j \quad (11)$$

where S_i is the Raman signal, E is the laser pulse energy, K_{ij} is the calibration coefficient matrix, and N_j is the major species number density. Flame temperatures were then derived from the ideal gas law. Two sets of spectra are juxtaposed to create the full spectrum for each linear scan. Methodology for removal of cosmic rays and background subtraction are discussed in detail in reference [7]. Throughout the experiment, chemiluminescence images are observed and recorded using a PI-Max 4 (1024 x 1024) ICCD with an UG-11 filter to determine correct orientation, steady-state, and Raman scanning location.

Experimental calibration is performed with a 12.5 mm diameter Hencken burner. Species concentrations and temperatures are calculated using Cantera [33], assuming the measurement location, 15 mm above the burner, has reached adiabatic equilibrium. Calibration trials are chosen to determine interference factors and signals for all major species (CO_2, O_2, N_2, H_2O, and H_2) across a range of temperatures from 300 K to 2000 K. Reactant gas flow rates are controlled with flow controllers (Teledyne Hastings HFC-202/203) and co-flow gas rates are monitored with flow meters (Teledyne Hastings HFM-201). Flow controllers and meters are accurate to 1% full scale and were verified by laminar flow elements.

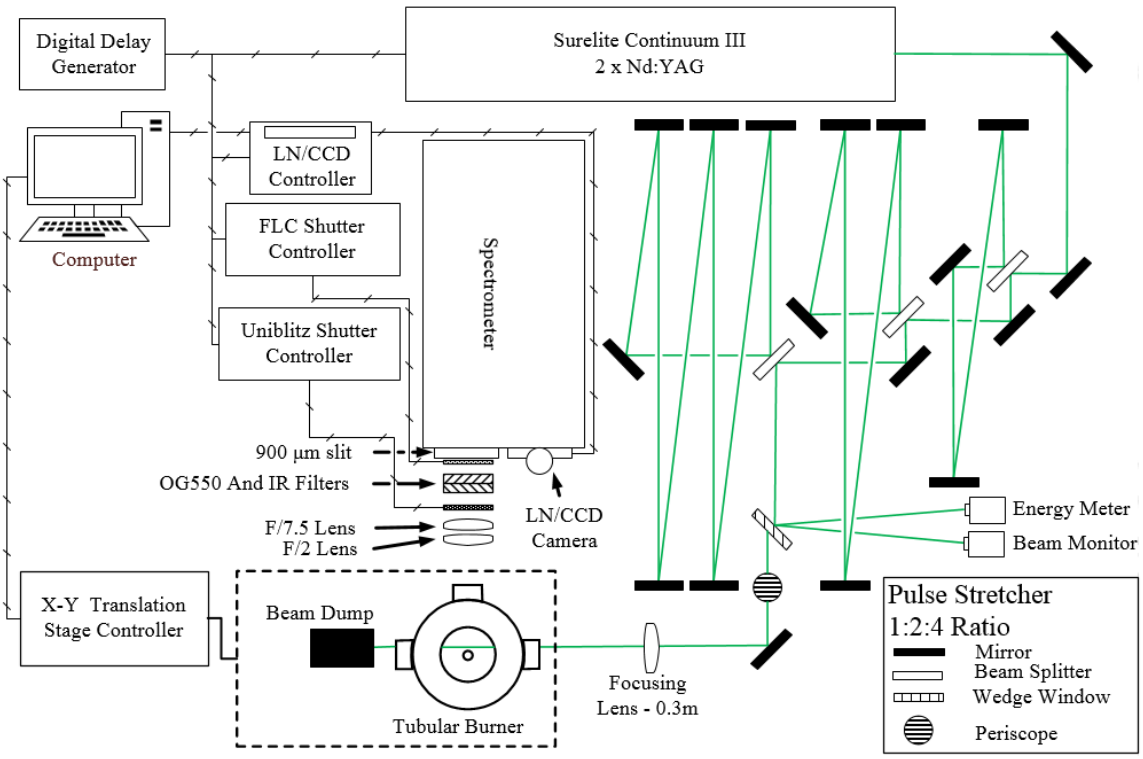

Figure 17 - Detailed schematic of Raman spectroscopy system

3.2. 8-CELL FLAME $\Phi = 0.235$, $\kappa = 100\ s^{-1}$

A flame structure containing premixed singular cells and a non-cellular diffusion flame was examined. For this case, incoming conditions were outer nozzle gases premixed at $\phi = 0.235$, $k = 100\ s^{-1}$, and volumetric dilution of 6:1 (CO_2:H_2) from the inner nozzle. The planar measurement of temperature and major species are shown in Figure 18. The laser beam is horizontal, enters from the right, and is scanned from bottom to top.

A direct numerical simulation, with inlet conditions as listed in Table 1, is compared to the experimental conditions using the model previously described [6, 7] with modifications to include the central fuel nozzle. Good agreement is found under most major species and the calculated equivalence ratio as shown in Figure 19. Minor discrepancies exist for temperature and H_2O results, with the simulation over predicting temperatures with N_2 as the primary diluent and under predictions for CO_2 as the primary diluent. These discrepancies are feasibly due to three body reaction rates within the mechanism used, but may be due to signal interference from the laser

beam scattering from the inner nozzle as mentioned in the following case. Radial profiles, interpolated to experimental resolution of 86μm, are found in Figure 19 and compare numerical and experimental results.

Adiabatic flame temperatures for the incoming mixture, $\phi = 0.235$, are 1020 K as compared to experimental values that exceed 1500 K and numerical results near 1300 K for cellular flames. Local enhancement of cells by preferential diffusion raises the peak equivalence ratio and subsequently the temperatures for combustion.

Table 1 - Nozzle boundary conditions for simulations of a flame with $\phi = 0.235$, $k = 100\ s^{-1}$. Concentrations are in mole fractions.

	W (1/s)	Temp. (K)	Exit Velocity (cm/s)	CO_2	H_2	O_2	N_2
Inner Noz.	0	295	15.9	0.86	0.14	0	0
Outer Noz.	40	295	36.2	0	0.090	0.19	0.72

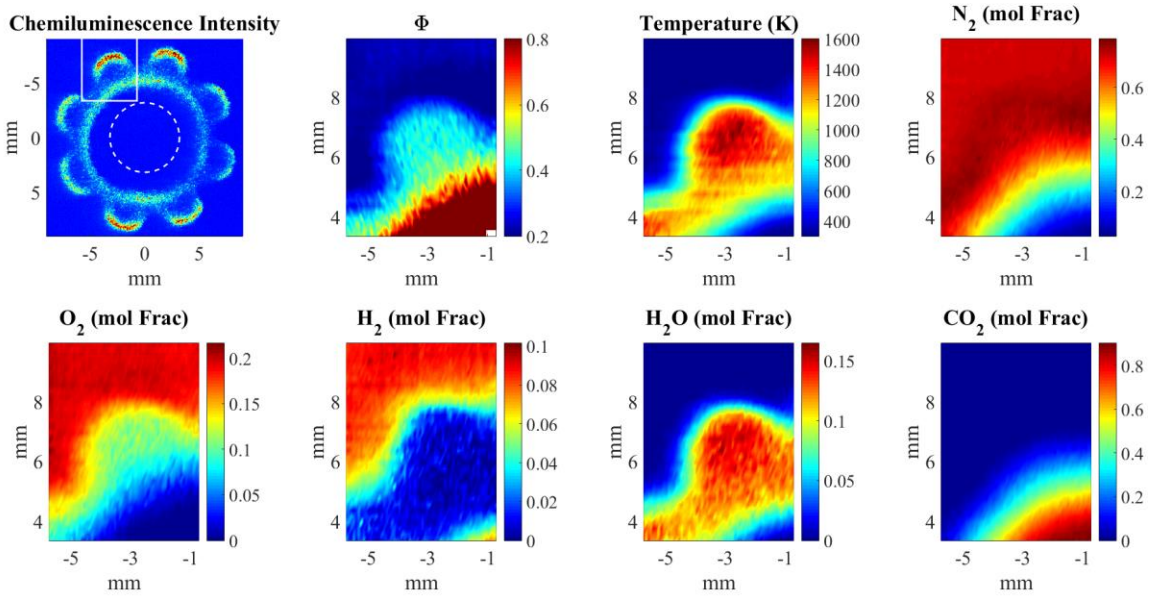

Figure 18 - 2D maps of temperature, major species, equivalence ratio and chemiluminescence. Raman scattering data is shown above for an incoming mixture with $k = 100\ s^{-1}$, $\phi = 0.235$, and constant fuel volumetric dilution ratio of CO_2:H_2 = 6:1. The chemiluminescence image shows the scanning region within the solid lined box. The dashed line shows the inner nozzle location. Scans are taken linearly from bottom to top with the laser incoming from right to left. Significant background interference impacts results near and in front of the inner nozzle.

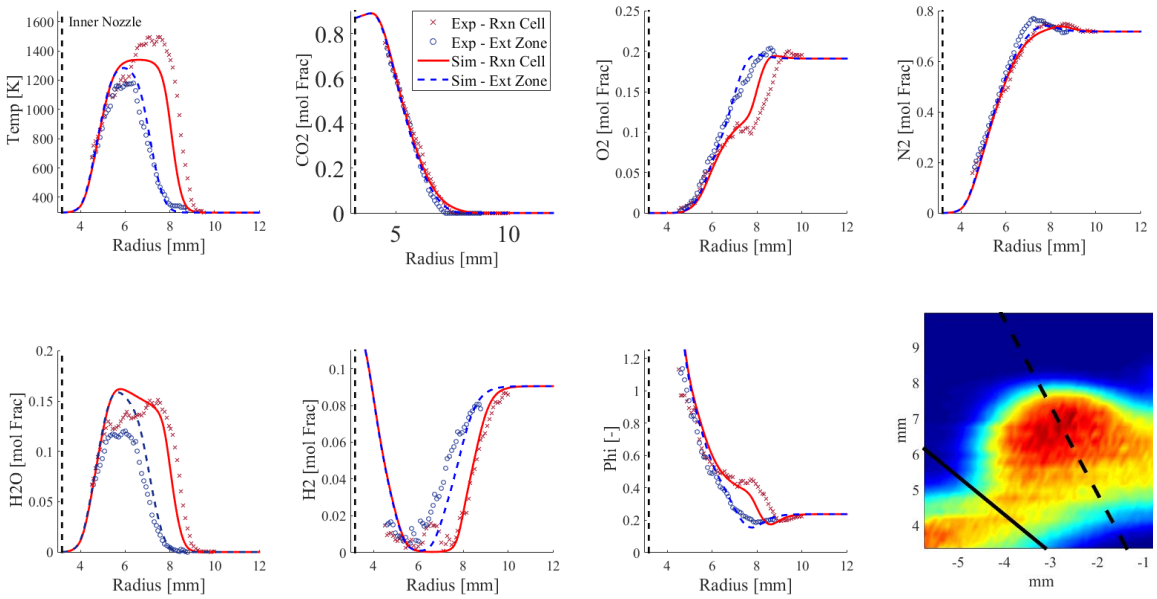

Figure 19 - Experimental and numerical radial profiles for temperature and major species. The data here is for an incoming gas mixture with k = 100 s^{-1}, ϕ = 0.235, and constant fuel volumetric dilution ratio of CO_2:H_2 = 6:1. The inner nozzle is shown by a vertical dashed line at 3.175 mm. Locations of radial slices are shown in the temperature image on the bottom right. The dashed line denotes the extinction cell and the solid line denotes the reaction cell.

3.3. 12-Cell Flame Φ = 0.271, κ = 128 s^{-1}

For the twelve cell case, incoming conditions from the outer nozzle gases were premixed at ϕ = 0.271, k = 128 s^{-1}, and volumetric dilution of 6:1 (CO_2:H_2) from the inner nozzle. A planar measurement of temperature and major species as shown in Figure 20.

A direct numerical simulation, with inlet conditions as listed in Table 2, is compared to the experimental conditions in Figure 21. For this case, all major species and temperature profiles have good agreement with the numerical results, except H_2O peak values, within the diffusion flame. Discrepancies are significantly less than that of the eight cell case and attributed to the measurement zone being almost entirely tangent to the edge of the inner nozzle and far in radius. Moving the scanned region in the positive x-direction (to the right) produces significant background interference, caused by laser reflections off the inner nozzle, and restricts the quantity

and quality of data that can be obtained. Radial profiles, interpolated to experimental resolution of 86μm, are found in Figure 21 and compare of numerical and experimental results.

Table 2 - Nozzle boundary conditions for simulations of a flame with $\phi = 0.271$, $k = 128\ s^{-1}$. Concentrations are in mole fractions.

	W (1/s)	Temp. (K)	Exit Velocity (cm/s)	CO_2	H_2	O_2	N_2
Inner Noz.	0	295	15.85	0.85	0.15	0	0
Outer Noz.	65	295	51.49	0	0.105	0.19	0.72

Adiabatic flame temperatures for the incoming mixture, $\phi = 0.271$, are 1120 K as compared to experimental and numerical values that exceeding 1400 K for cellular flames. Once more, preferential diffusion of hydrogen toward the reaction zone increases the equivalence ratio and temperatures. It is expected that the model performs accurately given the experiments conducted here and understanding of signal interferences due to experimental restrictions.

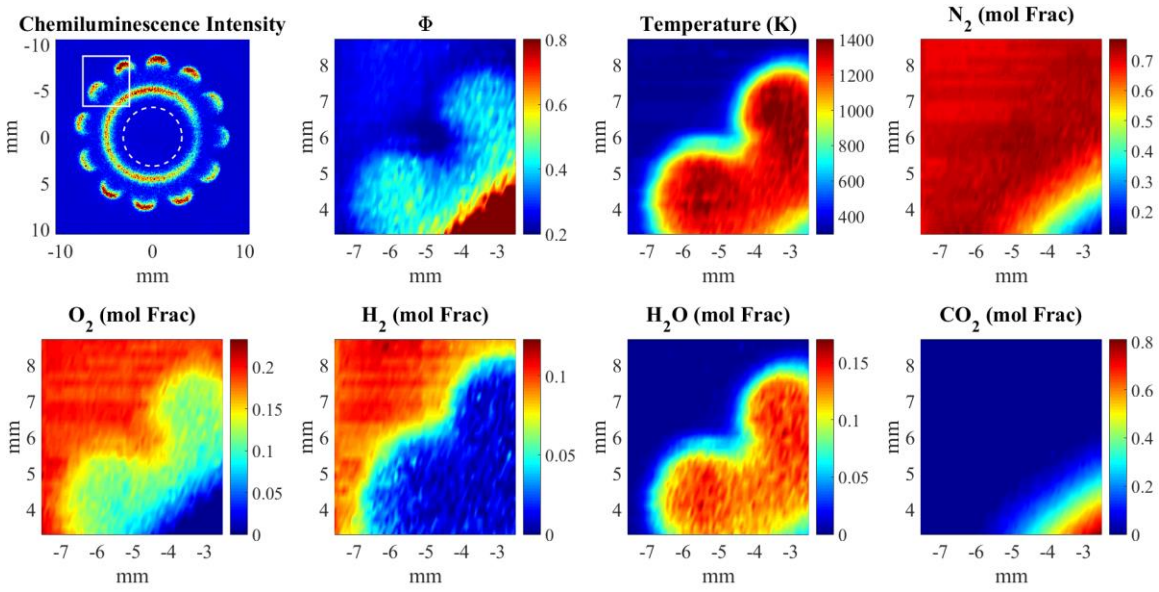

Figure 20 - 2D maps of temperature, major species, equivalence ratio and chemiluminescence. Data collected via Raman scattering is shown above for a flame with $k = 128\ s^{-1}$, $\phi = 0.271$, and constant fuel volumetric dilution ratio of CO_2:H_2 = 6:1. The laser line is from right to left. The scanning pattern moves from bottom to top. The chemiluminescence image shows the scanning region within the solid lined box. The dashed line shows the inner nozzle location

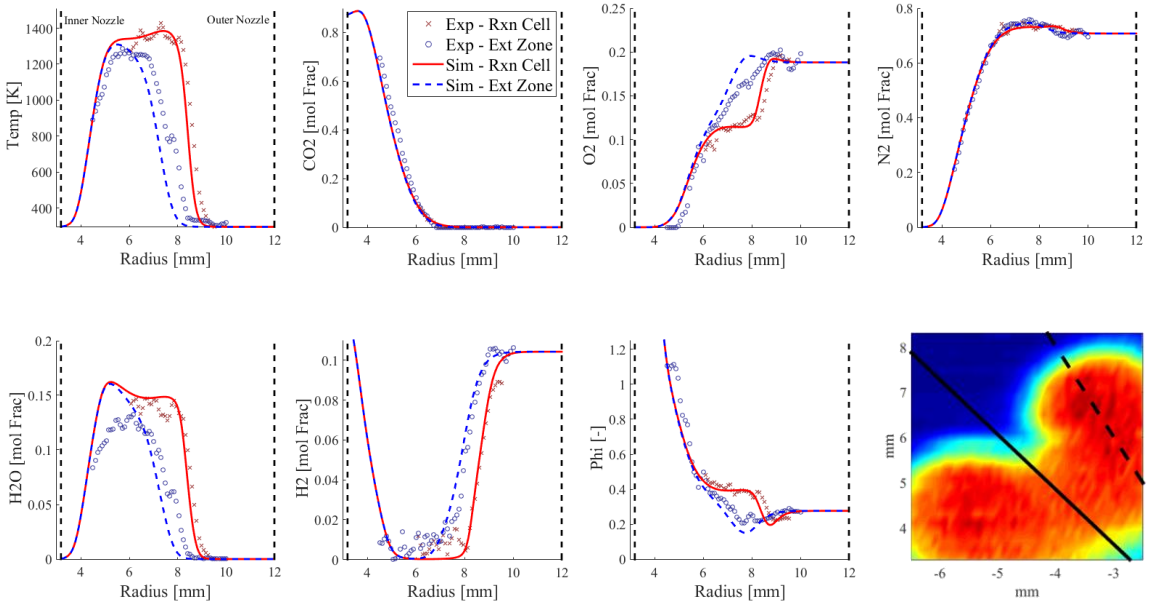

Figure 21 - 1D interpolated radial profiles and location. The temperature image (bottom right) contains markings for radial profile interpolations. The dashed line denotes a reaction cell and the solid line an extinction zone. The data here is for a PPTF with k = 128 s^{-1}, ϕ = 0.271, and constant volumetric fuel dilution ratio of CO_2:H_2 = 6:1. The inner nozzle is shown by a vertical dashed line at 3.175 mm

3.4. SPLIT-CELL FLAME $\Phi = 0.292$, $K = 96\ s^{-1}$

A partially premixed tubular flame containing both premixed split-cell structures and singular-cell structures as well as a non-cellular diffusion flame was investigated using Raman scattering and is shown in Figure 22. Numerical simulations of split-cell flames have not been achieved due to time constraints. Adiabatic flame temperatures for the incoming mixture are near 1170 K, the split cell temperatures fluctuate around 1220 K across the cell, peaking around 1300 K by the non-reacting cusp. The cell curvature appears large in comparison to single cell curvature, leading to lower influence of preferential diffusion. In both prior cases of singular cells, the flame temperature was enhanced more than 50% above of the adiabatic flame temperature for the incoming mixture, enhancement of the split cell was only 15 - 20% above the incoming mixture.

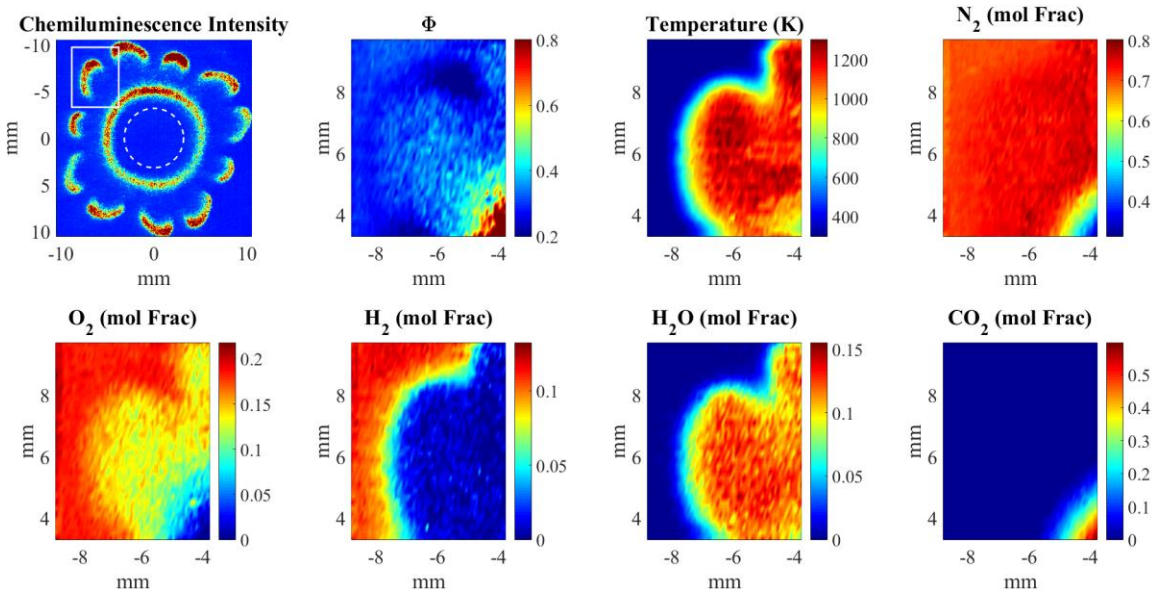

Figure 22 - 2D maps of temperature, major species, equivalence ratio and chemiluminescence. Data collected via Raman scattering is shown above for a flame with k = 96 s^{-1}, ϕ = 0.292, and constant fuel volumetric dilution ratio of CO_2:H_2 = 6:1. The laser line is from right to left. The scanning pattern moves from bottom to top. The chemiluminescence image shows the scanning region within the solid lined box. The dashed line shows the inner nozzle location.

3.5. NUMERICAL ANALYSIS

A substantial advantage of numerical work is the reduced costs for experimentation and the ability to view information that cannot readily or realistically be measured. Experimental campaigns in this research were paralleled with numerical simulations to determine the ability of the code to match qualitative results of chemiluminescence in addition to quantitative data from Raman spectroscopy as previously discussed.

Details regarding the numerical method and setup are found in reference [7], and performed under nearly identical processing power. Full 2-π domain simulations for partially premixed flames require approximately ten hours on average with good initial conditions. A parametric study was initiated to study increasing premixing from the outer nozzle as performed by chemiluminescence in Section 2.3. A non-cellular to cellular transition is shown in Figure 23, showing H-atoms which have high similarity to chemiluminescent response. The transition from eight to ten cells (ϕ = 0.250 → 0.255→ 0.260, k = 90 s^{-1}) did not occur smoothly as expected.

Instead, an intermediate steady-state solution was formed with partial cells barely extending from the diffusion flame as seen in Figure 24, similar to chemiluminescent data. Despite mismatches in the position of cells, the likeness between each structure is promising for future work. Higher transition states used the maximum RAM available and required significant time for computations, reducing the ability for extended analyses, yet valuable information was gained regarding computational ability for transition states, and qualitative accuracy.

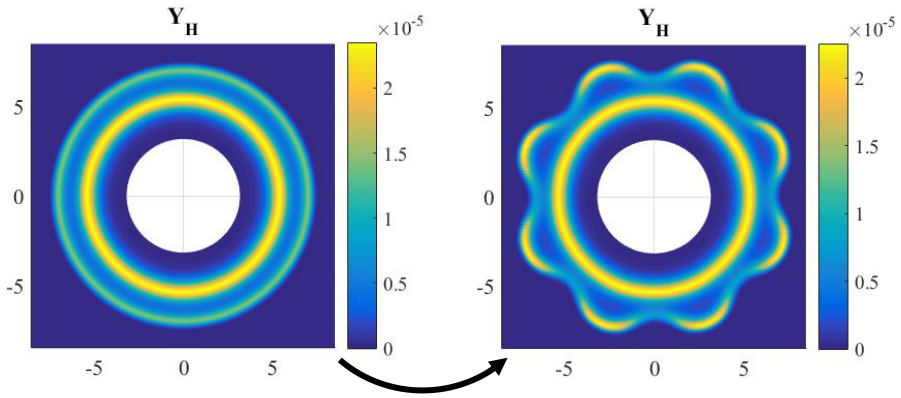

Figure 23 - Hydrogen atom results for a full 2- π domain simulation of a transition from non-cellular to an 8-cell flame structure with k = 90 s^{-1} across ϕ = 0.230 (left) to ϕ = 0.235 (right), the RAM required during computations, and total solve time by a five computer cluster

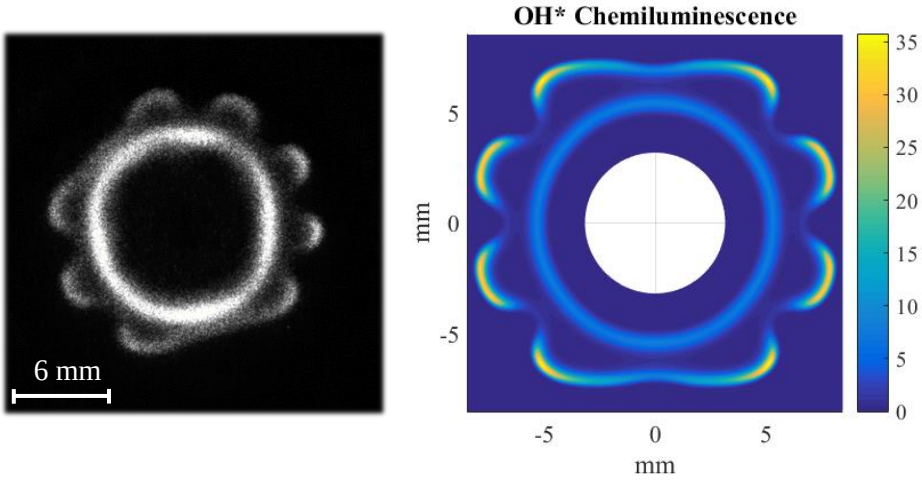

Figure 24 - Chemiluminescent image (left) of an 8-cell steady-state flame between non-cellular and cellular states (see Figure 11), and OH* chemiluminescence values of steady-state direct numerical simulations of an 8-cell to 10-cell transition from ϕ = 0.250 to ϕ = 0.255. Partial cells as shown in both results here are uncommon in both numerical and experimental work performed here

3.6. AXIAL VELOCITY GRADIENT (W) BOUNDARY CONDITION

Accuracy of numerical solutions is strongly dependent on proper boundary conditions. In opposed jet flames, nozzles can produce non-zero velocity gradients at the nozzle exits that can affect model-data comparisons [34, 35, 36], and there has been little work in investigating nozzle effects in tubular burners [37]. Published work on stagnation flow burners have shown the gradient boundary condition to be positive and non-zero for contoured nozzles [38]. For previous simulations of cellular tubular flames [1, 3], the axial velocity gradient at the outer nozzle exit of the simulations was adjusted to obtain the best correspondence of the experimental and simulated flame position. The axial velocity gradient (W) is the expansion or contraction of flow along the axial coordinate, also known as the stretch or strain rate, and is expressed as,

$$W = \frac{du_z}{dz} \tag{9}$$

Despite a plethora of experimental data available for tubular burners, many questions remain. Various laser diagnostic techniques have been performed on tubular flames ranging from pure premixed to pure diffusion flames [39, 40], and have been used as a baseline for comparison to simulations. However, the results from these techniques are limited to temperature and species profiles, leaving questions regarding fluid dynamic boundary conditions unanswered. Progress has recently been achieved toward full chemical kinetic and transport combustion simulations of tubular laminar flames, using an in-house code with respect to premixed and diffusion flames; prior work shows good agreement for diffusion and premixed flames with respect to temperature fields and species concentrations [7]. Partially premixed simulations using the same code showed high sensitivities to the W boundary condition and require further investigation to continue progress efficiently.

Simulations were performed for a PPTF with $\phi = 235$, $k = 90\ s^{-1}$ with the axial velocity gradient (W) varying from 20 to 90 s^{-1}. Full nozzle boundary conditions are listed in Table 3, and

a 2D image showing the location 1D profiles is shown in Figure 25. The effects of varying the axial boundary condition were mainly translational, with minor impacts on the peak values of major species concentrations and temperature profiles as shown in Figure 26. Peak temperatures fluctuated by less than 50 K between cases shown here. Clear translations of major species and temperature gradients approach 1 mm in the premixed cells and less than 0.5 mm in the diffusion flame. Due to different effects on each flame, higher values for the axial velocity gradient boundary condition produced thicker flames, and lower values thinner flames.

The true effects of the boundary condition are found in minor species calculations, experiencing similar translation effects as well as deviance in concentration levels as shown in Figure 27. For lower W values, thinner flames, minor species concentrations increased in both premixed and diffusion flame zones. Higher W values produced thicker flames and thus lower concentrations. These variations show that understanding the axial velocity gradient is paramount to accurate simulations of partially premixed tubular flames.

Table 3 - Nozzle boundary conditions for parametric sweep of the axial velocity gradient (W) from values of 20 to 90 s^{-1} with ϕ = 235, k = 90 s^{-1}

	W (1/s)	Temp. (K)	Exit Velocity (cm/s)	CO_2	H_2	O_2	N_2
Inner Noz.	0	295	15.9	0.86	0.14	0	0
Outer Noz.	*	295	36.2	0	0.090	0.19	0.72

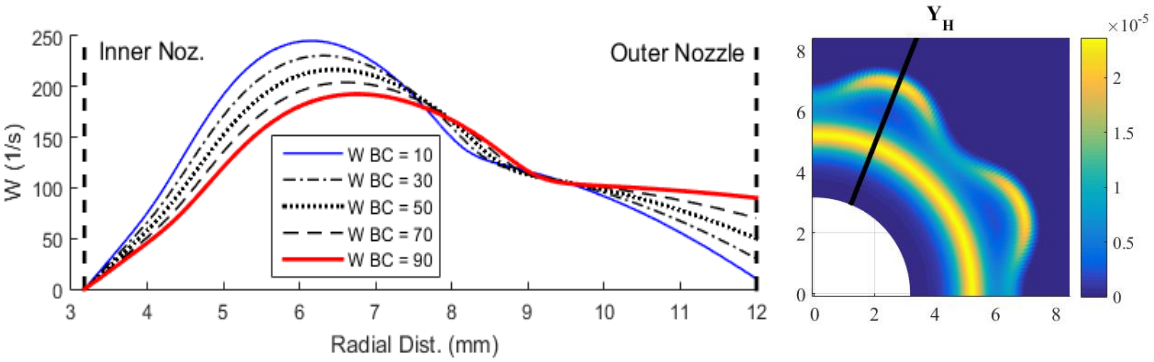

Figure 25 - Simulation profiles as a function of the axial velocity gradient boundary condition along a radial line of a partially premixed reaction cell with ϕ = 0.235, k = 90 s^{-1}. The profiles correlate with the centerline of a reaction zone in the flame, shown on the right, and translate significantly and have large differences in peak values due to the boundary condition.

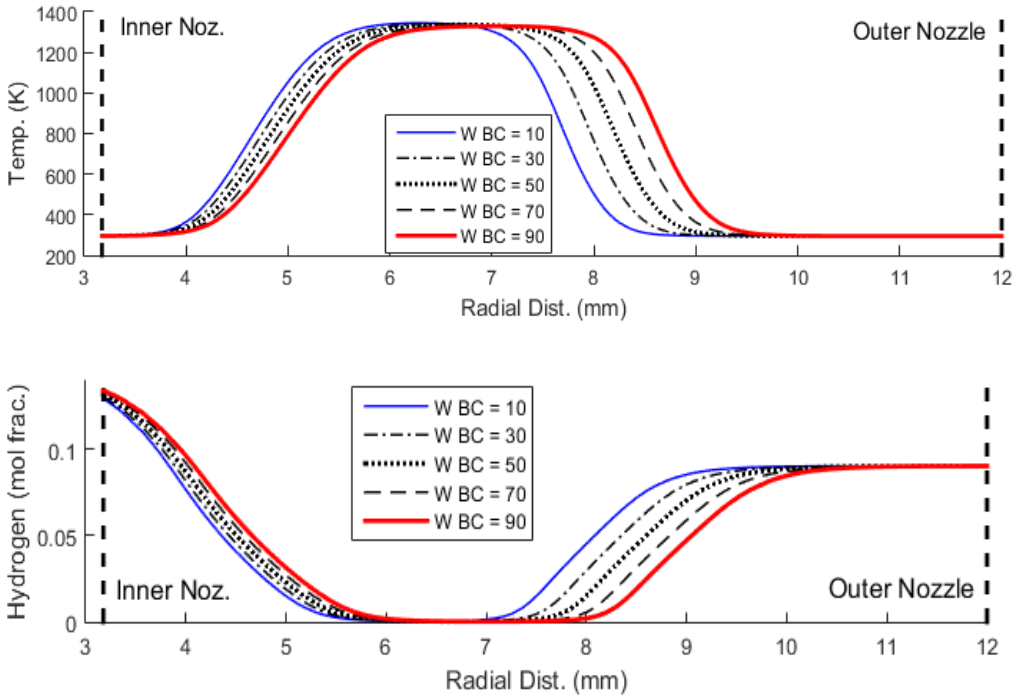

Figure 26 - Simulation profiles for temperature and hydrogen along a radial line of a partially premixed reaction cell with $\phi = 0.235$, $k = 90\ s^{-1}$. Larger values for W produce thicker flames with lower peak axial velocity gradients, but do not affect peak values for temperature

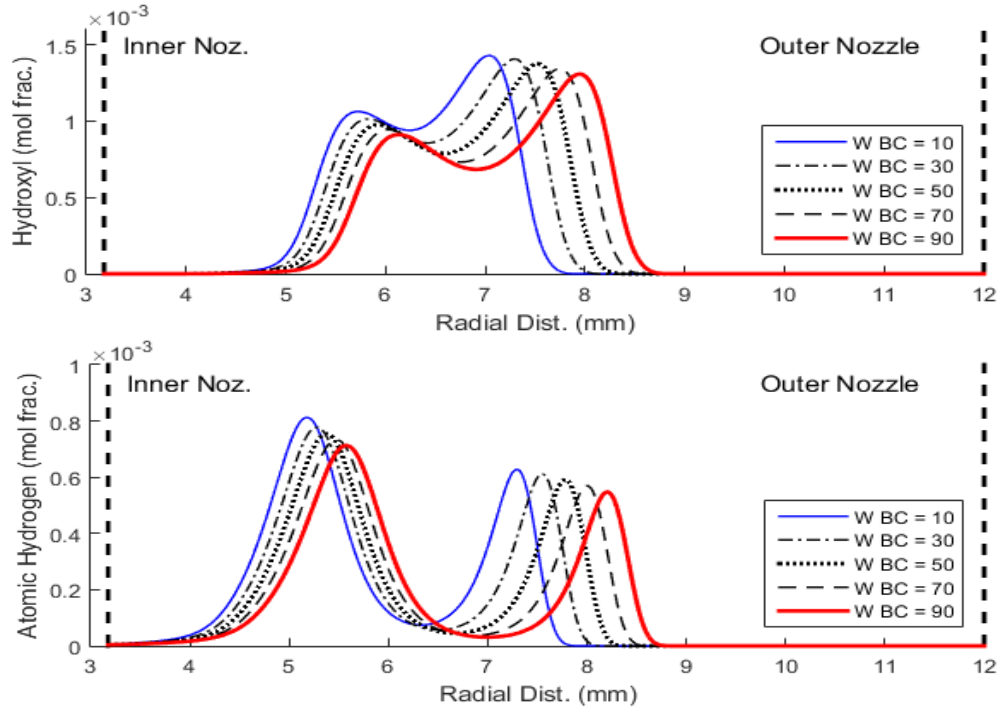

Figure 27 - Simulation profiles for hydroxyl and atomic hydrogen along a radial line of a partially premixed reaction cell with $\phi = 0.235$, $k = 90\ s^{-1}$. Lower axial velocity gradients create a thinner flame with higher peak values for minor species.

3.6.1. AXIAL VELOCITY GRADIENT (W) COMSOL ANALYSIS

To provide a starting point for the boundary condition, a 2D axial-symmetric COMSOL simulation was performed for cold-flow with boundary conditions replicating conditions used in the in-house simulation at Vanderbilt. The modeling approach used *Laminar Flow* physics to develop initial conditions for fluid dynamics by solving the continuity equation and the Navier-Stokes equations for conservation of momentum. The results are fed into a *Reacting Flow* model, which adds convective and diffusive transport equations, and uses concentrated species with N_2 as the mass constraint.

The model used is shown in Figure 28 and was produced from a cross section of the CAD model (see Figure 4) used to manufacture the burner. The model is axial symmetric from an offset symmetry line 3.175 mm from the left boundary to represent the inner nozzle. To reduce computational time, flow outside of the reaction zone is cut off 27 mm above the coflow entrance of the outer nozzle. Flow above and below this line is exhausted into the room and does not influence behavior upstream.

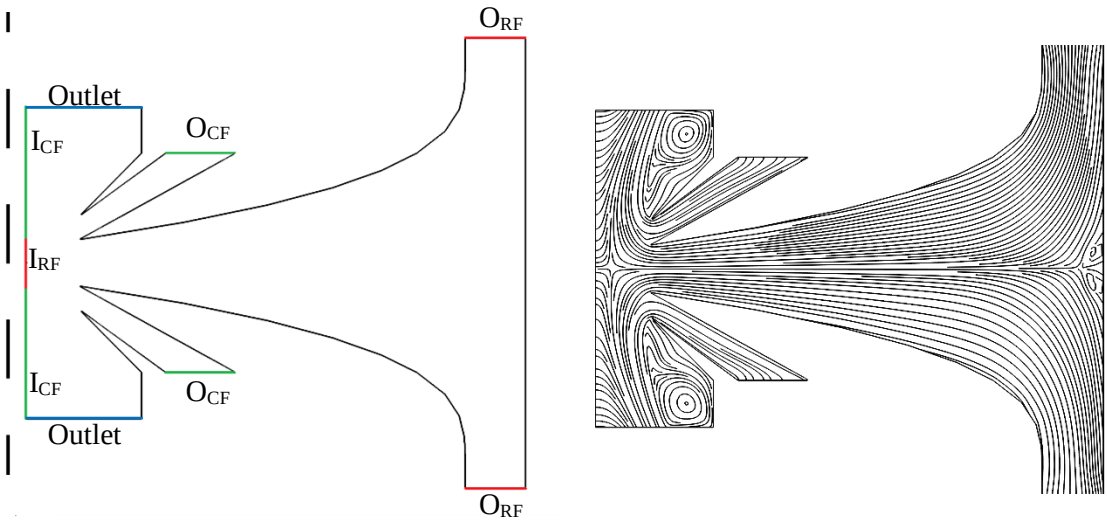

Figure 28 - A 2D axial-symmetric COMSOL model is on the left with blue lines representing outlet/outflows, red lines indicating reactant inlet/inflows, and green lines representing coflow inlet/inflows. Streamlines of cold-flow at k = 90 s^{-1} are shown on the right with coflow and reactant bulk velocities at the nozzle exits set as equal.

The global parameter list is given in Table 4 and represents the boundary conditions fed into the model for flow velocities, molar masses, and species concentration at inlets. These conditions represent a cold-flow mixture for a partially premixed flame with a dilution ratio of 16% H_2 from the inner nozzle, k = 90 s^{-1}, and ϕ = 0.235. Mixture specifications for inlets were set at 10^{-4} for gases not listed in the Table 4. As N_2 is the mass constraint for the reacting flow model, it is not listed as a boundary condition for the outer nozzles. The mole fraction for N_2 is calculated by subtracting all boundary conditions from unity. Thus, the outer nozzle had 0.9996 mol N_2 as calculated by the conservation of mass.

Table 4: Global Parameter List

Name	Expression		Description
O_R	2.14	[cm/s]	Outer Nozzle Reactant Velocity
O_CF	*	[cm/s]	Outer Nozzle Coflow Velocity
I_R	15.9	[cm/s]	Inner Nozzle Reactant Velocity
I_CF	15.9	[cm/s]	Inner Nozzle Coflow Velocity
T_Amb	293.15	[K]	Ambient Temperature
M_CO_2	44.01	[g/mol]	Molar Mass of CO_2
M_H_2O	18.02	[g/mol]	Molar Mass of H_2O
M_N2	28.01	[g/mol]	Molar Mass of N_2
M_H_2	2.01	[g/mol]	Molar Mass of H_2
M_O2	32.0	[g/mol]	Molar Mass of O_2
IN_x_H_2	0.14	[-]	Inner Nozzle Mole Fraction of H_2
IN_x_CO_2	0.86	[-]	Inner Nozzle Mole Fraction of CO_2
ON_x_O_2	0.21	[-]	Outer Nozzle Mole Fraction of O_2

Table 5: Variable List

Name	Expression		Description
w_p1	$r * u_r \frac{d\rho}{dr}$	[kg/(m^2/s)]	Term 1
w_p2	$\rho(u_r + r\frac{du_r}{dr})$	[kg/(m^2/s)]	Term 2
w_p3	$u_z \frac{d\rho}{dz}$	[kg/(m^2/s)]	Term 3
axl.vel.grd	$\frac{\left(\frac{1}{r}\right)(w_{p1}+w_{p2}+w_{p3})}{\rho}$	[1/s]	Axial Velocity Gradient

The mesh for the model was calibrated for fluid dynamics and set to the predefined *Finer* settings across the entire geometry. Custom refinement was performed along the burner

centerline, outer nozzle exits, and select boundaries outside the nozzles. The maximum element size was reduced to 500 μm, the minimum element size was set to 0.5 μm, and the maximum growth rate was set at 1.02. Curvature and resolution of narrow regions were set at the default *Extremely Finer* settings of 0.2 and 1 respectively. The mesh quality is shown in Figure 29 with the maximum element size near 2.5 mm and a minimum element size at 0.5 μm.

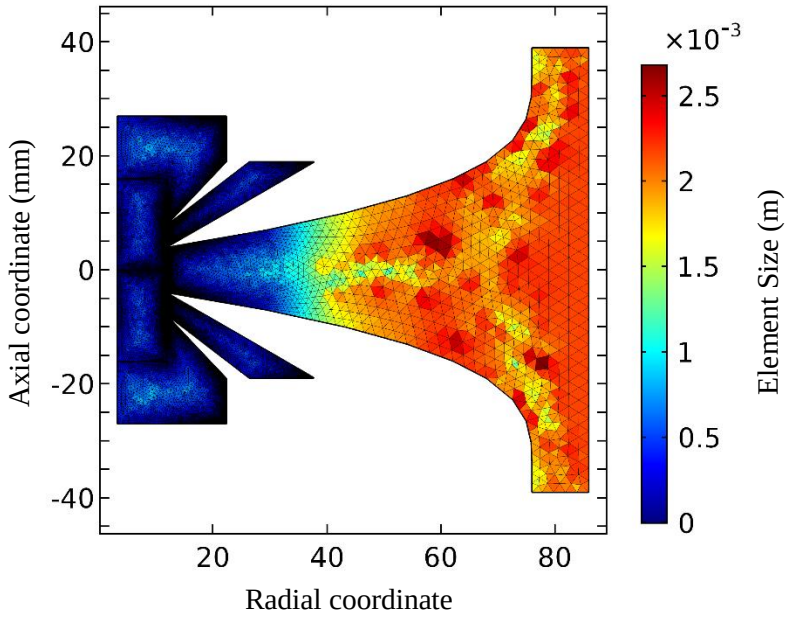

Figure 29 - Mesh quality for the tubular burner model

Other Modifications

All inlets have normal velocity fields entering the horizontal boundaries shown in Figure 28. During initial trials, COMSOL encountered divergence errors with the outer coflow inlet. The error was determined to be a singularity problem where the mesh could not resolve flow at the acute angle of the inlet. Design modifications used to avoid the error are shown in Figure 30. Image 1 of Figure 30 shows the original geometry, and adding a 0.1 mm fillet produced image 2. For low speeds, COMSOL converged, yet realistic velocities produced divergence errors. A right-angle chamfer was combined with a fillet of diameter 0.1 mm to produce image 3. The third iteration converges for COMSOL with both realistic and excessively high inlet velocities.

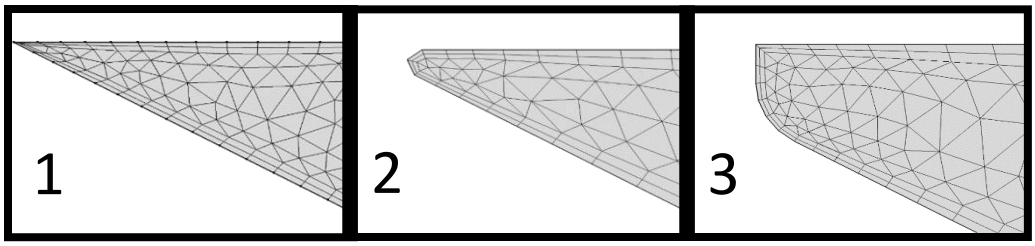

Figure 30 - The acute angle of inlet 2 is shown in image 1. Modification with a 0.1 mm fillet is shown in image 2. Modification with a 90 degree chamfer and 0.1 mm fillet is shown in image 3. COMSOL successfully converges the flow field with image 3 for necessary velocities.

The purpose of the coflow is to help create a uniform and known flow field by preventing entrainment of ambient gases and reducing the shear layers on the edges of the reacting flow. During experimentation, the coflow is typically set at the same standard flow rate as the reacting flow rate to match bulk velocities at the nozzle exits. Sensitivity of the boundary condition to the coflow velocity was examined by sweeping from half of the ideal velocity to twice the value (2.14, 4.28, 6.42, 8.56 cm/s). The results are shown in Figure 31, which should be compared qualitatively to Figure 25 for reacting flows. Peak values are scattered near the stagnation radius and see greater discrepancies by multiples of three to four times greater in reacting flow cases. The difference in the reaction zone is expected due to increased temperatures and lower densities caused by combustion. In both cold-flow and reacting cases, the axial velocity gradient converges near 9 mm along the radius. However, the reacting flow is nearly 50% greater for the ideal cold-flow case. Once more, differences in density are expected, but the hypothesized source of deviation is due to back-pressure created by the reaction zone, which propagates upstream and shifts the boundary condition upward. The results from the cold-flow COMSOL simulation should be understood as the minimal value for the axial velocity gradient when performing simulations with the in-house code at Vanderbilt.

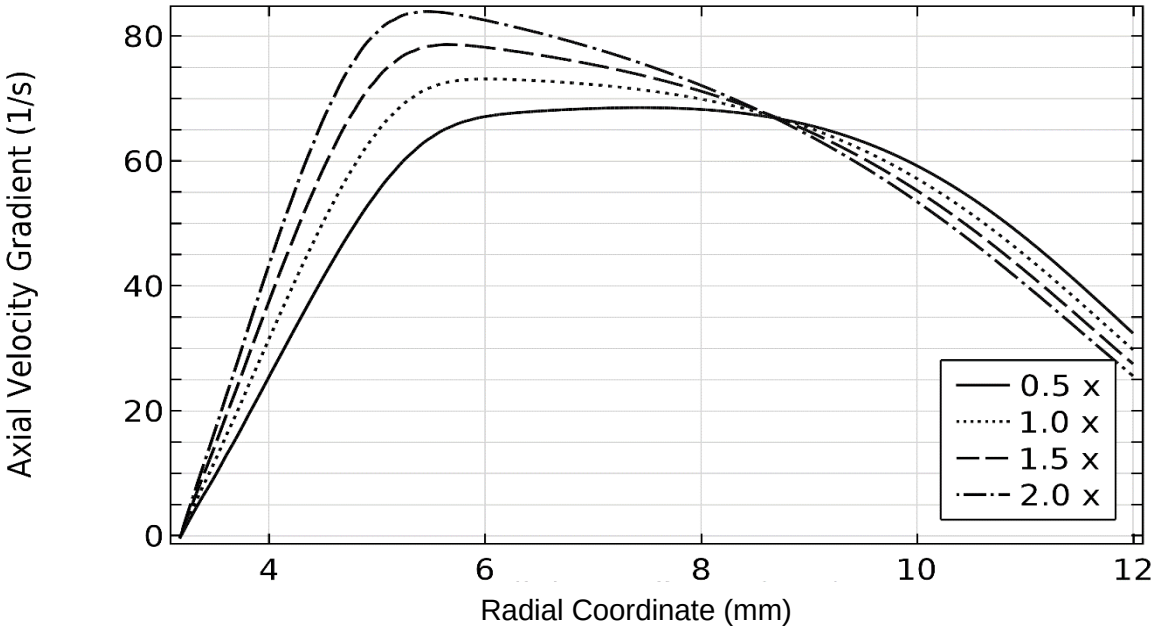

Figure 31 - Axial velocity gradient vs. radius for cold flow conditions at k = 90 s^{-1}. Plots represent outer nozzle coflow rates at 0.5, 1.0, 1.5, and 2.0 times the outer nozzle reactant flow rate at the nozzle exit.

CHAPTER 4:

CONCLUSIONS

Partially premixed flames were observed and studied for the first time in a tubular burner by means of chemiluminescence, Raman spectroscopy, and direct numerical simulation. For each method, conclusions follow.

4.1. CHEMILUMINESCENCE

Parametric surveys were conducted from limits of flashback to flame extinction for low to moderate stretch rates, and produced novel hybrid flame structures with characteristics of both premixed and diffusion tubular flames. Dominating instabilities in hybrid flames with both premixed and diffusion characteristics were (1) cellular, (2), vibrational, and (3) rotational. A new structure of steady-state cellular instabilities was discovered, aptly named "split cells" due to paired formation. Partially premixed structures containing any multiple of split cells have been called "star-shaped" flames, while those containing only single cell structures have been called "flower-shaped" flames.

Rotational instabilities were primarily caused by misalignment of the inner-nozzle, but were found even after tedious alignment for select cases. Regardless of presence of rotational instabilities, flower-shaped flames were exceptionally stable and resistant to mechanical perturbations of the flow field by a wire. Vibrational instabilities were observed near transition points of the flame structure where the cell count would fluctuate. Cells expanded and contracted at near constant rates acting primarily in the theta direction, and marginally in the radial direction.

Cellular flames were found primarily in premixed flame structures, but also existed in lean premixing cases that closely resembled pure diffusion flame cells. Equivalence ratios near 0.275 produced clearly defined cellular and non-cellular, steady-state flame structures. Cellular flames were entirely separate from the diffusion flame structures, and only became dependent on the

diffusion flame when split cells formed. In addition, across all fuels and inlet conditions, single-cells structures had little dependence on burning intensity of the diffusion flame suggesting a superposition of premixed and diffusion flames, while split cells had strong dependence on existence and behavior of the diffusion flame

Variation in premixing produced the largest variation in flame structure and cellular formation, with unique structures forming near flashback conditions. For all cases, flames were more uniform with smaller stagnation radii due to consistent flow exiting the inner nozzle. While the premixed cell structure saw some dependency on the stagnation radius, no quantitative results were found to predict the overall flame structure or interactions between premixed and diffusion flames due to the stagnation radius by investigations in this study.

Small hydrocarbon diffusion flames with Lewis numbers away from unity were examined and produced cellular flames in both premixed and diffusion flame zones, unseen in prior tubular flame literature. Methane-H_2 flame structures with such has single premixed cells with an associated diffusion cell across a small range of fuel-dilution rates. In addition to structures seen in Methane-H_2 flames, diffusion flame structures in Propane-H_2 flames experienced breaks between split cells to create a small radial path where no chemiluminescence was observed.

4.2. RAMAN SPECTROSCOPY

Three partially premixed tubular flames were examined using Raman spectroscopy with structures containing 8-cell, 12-cell, and split-cell flames. Single cells experienced temperature enhancement near 50% above the adiabatic temperature for combustion of the incoming mixtures, whereas temperature of the split cells were only 15-20% higher. The larger curvature of the split cells indicates lower preferential diffusion, which supports the lower temperature enhancement. The largest improvement to data quality provided by the current experimental method would be gained by reduction of shutter speed by replacing the FLC and Uniblitz shutters with one slow and one fast rotating chopper shutter and a single opaque leaf shutter. Other diagnostic methods

with a larger field of view would be highly beneficial to understanding these flames due to the structure size.

4.3. NUMERICAL

The current limitations for computational power are 19 cores with 60 GB RAM, which is able to simulate a significant amount of cases observed. More experimental data should be taken to validate the model across different equivalence ratios and stretch rates, and determine the cause of inconsistencies in H_2O values. It is expected that variation in recombination rates will account for these differences. Good alignment was found between the in-house code at Vanderbilt and Raman spectroscopy data collected. The largest discrepancies were found for H_2O for the radial locations along the diffusion flame. Simulation results produced values approximately 50% higher than experimental results. All other major species aligned well for peak values and gradients. Temperature inconsistencies existed for the 8-cell case and are attributed to scattering from the inner nozzle.

The axial velocity gradient boundary condition at the outer nozzle has been shown by numerical comparisons to influence the flame thickness and peak values of minor species. Due to use of the parameter for tuning, experimental measurements within a tubular are of paramount importance. Experimental limitations have prompted cold-flow simulations by COMSOL, and produced results showing an increase in the coflow velocity decreases the axial velocity gradient boundary condition, but causes a higher peak value. Experimental sensitivity to coflow velocities is low as a 50% change in coflow velocity causes a 10% deviation at most and near the peak values. Deviations appear linearly correlated to coflow velocity increase, as a velocity increase by 100% causes a 20% deviation. The trends and values produced by the COMSOL model have good qualitative alignment with the results from the in-house code at Vanderbilt, especially when accounting for density changes within the reacting flow.

CHAPTER 5:

FUTURE WORK

The novelty of flame structures found with partially premixed tubular flames necessitates further studies. First and foremost, detailed investigations of the axial velocity gradient and/or affected measurables should be taken to reduce simulation tuning and improve accuracy of future results. Consequently, experimental studies of minor-species offers great benefit for future numerical work and understanding of the flame behavior as a whole, and can act as a guide to tuning the model given sensitivity to the axial velocity gradient.

Further experimental work can be performed on effects of stretch and curvature, and evaluation of star-shaped flames with split cells is advised due to the wide range of curvatures offered in a single experimental trial. These structures are expected to be highly sensitive to thermal-diffusive transport properties as well and offer a strong case for validation of numerical results. Due to the discovery of double-cellular tubular flames, both qualitative and quantitative examination of small hydrocarbon flames will offer strong cases for analyzing effects of transport phenomena. Methane-hydrogen partially premixed tubular flames are within the computational power of the in-house code at Vanderbilt and should be analyzed alongside these studies. With appropriate computational resources, the same efforts should be put toward propane-air flames.

Further numerical work should focus on investigation of chemical kinetics on model accuracy, and discrepancies between current experimental and numerical results for H_2O should be resolved with the focus on recombination reactions. Lastly, refinement of boundary conditions used for the in-house code should be explored that successfully prevent rotational flow, without producing discontinuities within the pressure field.

REFERENCES

[1] S. Hu, *Measurements and modeling of non-premixed tubular flames: structure, extinction and instability. Ph.D. Thesis,* Nashville: Vanderbilt University, 2007.

[2] S. Ishizuka, "Determination of flammability limits using a tubular flame geometry," *Journal of Loss Prevention in the Process Industries,* vol. 4, no. 3, pp. 185-193, 1991.

[3] V. Yang, Liquid rocket engine combustion instability, vol. 169, Washington DC: Progress in Astronautics and Aeronautics, AIAA, 1995.

[4] K. R. McManus, T. Poinsot and S. M. Candel, "A review of active control of combustion instabilities," *Progress in Energy and Combustion Science,* vol. 19, no. 1, pp. 1-29, 1993.

[5] M. Matalon, "Intrinsic flame instabilities in premixed and nonpremixed combustion," *Annu. Rev. Fluid Mech.,* vol. 39, pp. 163-191, 2007.

[6] C. A. Hall and R. W. Pitz, "Numerical simulation of premixed H2–air cellular flames," *Combustion Theory and Modelling,* vol. 20, no. 2, pp. 328-348, 2016.

[7] C. A. Hall, *Instability of premixed lean hydrogen laminar tubular flames. Ph.D. Thesis,* Nashville: Vanderbilt University, 2016.

[8] R. B. Bird, W. E. Stewart and E. N. Lightfoot, Transport phenomena, revised 2nd edition, New York: John Wiley & Sons, Inc., 2006.

[9] Y. Wang, S. Hu and R. W. Pitz, "Extinction and cellular instability of premixed tubular flames," *Procceedings of the Combustion Institute,* vol. 32, no. 1, pp. 1141-1147, 2009.

[10] R. W. Pitz, S. Hu and P. Wang, "Tubular premixed and diffusion flames: effect of stretch and curvature," *Progress in Energy and Combustion Science,* vol. 42, pp. 1-34, 2014.

[11] F. Williams, "A review of flame extinction," *Fire Safety Journal,* vol. 3, pp. 163-175, 1981.

[12] P. Wang, J. A. Wehrmeyer and R. W. Pitz, "Stretch rate of tubular premixed flames," *Combustion and Flame,* vol. 145, no. 1-2, pp. 401-414, 2006.

[13] S. K. Aggarwal, "Extinction of laminar partially premixed flames," *Progress in Energy and Combustion Science,* vol. 35, pp. 528-570, 2009.

[14] A. R. Masri, "Partial premixing and stratification in turbulent flames," *Proceedings of the Combustion institute,* vol. 35, pp. 1115-1136, 2015.

[15] R. D. Lockett, B. Boulanger, S. C. Harding and D. A. Greenhalgh, "The structure and stability of the laminar counter-flow partially premixed methane/air triple flame," *Combustion and Flame,* vol. 119, no. 1-2, pp. 109-1210, 1999.

[16] P. Wang, S. Hu and R. W. Pitz, "Numerical investigation of the curvature effects on diffusion flames," *Proceedings of the Combution Institute,* vol. 31, no. 1, pp. 989-996, 2007.

[17] G. Dixon-Lewis, V. Giovangigli, R. J. Kee, J. A. Miller, B. Rogg, M. D. Smooke, G. Stahl and J. Warnatz, "Numerical modeling of the structure and properties of tubular strained laminar premixed flames," in *Dynamics of Deflagrations and Reactive Systems: Flames*, Washington, DC, American Institute of Aeronautics and Astronautics, 1991, pp. 125-144.

[18] D. M. Mosbacher, J. A. Wehrmeyer, R. W. Pitz, C. J. Sung and J. L. Byrd, "Experimental and numerical investigation of premixed tubular flames," *Proceedings of the Combustion Institute,* vol. 29, pp. 1479-1486, 2002.

[19] H. S. Bak, R. S. Lee, J. H. Chen and C. S. Yoo, "A numerical study of the diffusive-thermal instability of opposed nonpremixed tubular flames," *Combustion and Flame,* vol. 162, no. 12, pp. 4612-4621, 2015.

[20] S. W. Shopoff, P. Wang and R. W. Pitz, "Experimental study of cellular instability and extinction of non-premixed opposed-flow tubular flames," *Combustion and Flame,* vol. 158, no. 11, p. 2165–2177, 2011.

[21] C. Altantzis, C. Frouzakis, A. Tomboulides, M. Matalon and K. Boulouchos, "Hydrodynamic and thermodiffusive instability effects on the evolution of laminar planar lean premixed hydrogen flames," *J. Fluid Mech.*, vol. 700, pp. 329-361, 2012.

[22] Y. Wang, "Cellular instability phenomenon in premixed tubular flames and non-premixed opposed tubular flames," M.S. Thesis, Vanderbilt University, Nashville TN, 2008.

[23] S. Hu, P. Wang, R. W. Pitz and M. D. Smooke, "Experimental and numerical investigation of non-premixed tubular flames," *Proceedings of the Combustion Institute,* vol. 31, no. 1, pp. 1093-1099, 2007.

[24] S. Hu and R. W. Pitz, "Structural study of non-premixed tubular hydrocarbon flames," *Combustion and Flame,* vol. 156, no. 1, p. 51–61, 2009.

[25] G. I. Sivashinsky, "Instabilities, pattern formation, and turbulence in flames," *Annual Review of Fluid Mechanics,* vol. 15, pp. 179-199, 1983.

[26] E. G. Groff, "The cellular nature of confined spherical propane-air flames," *Combustion and Flame*, vol. 48, pp. 51-62, 1982.

[27] C. K. Law, G. Jomaasa and J. K. Bechtoldb, "Cellular instabilities of expanding hydrogen/propane spherical flames at elevated pressures: theory and experiment," *Proceedings of the Combustion Institute*, vol. 30, no. 1, p. 159–167, 2005.

[28] S. Ishizuka and C. K. Law, "An experimental study on extinction and stability of stretched premixed flames," *Symposium (International) on Combustion*, vol. 19, no. 1, pp. 327-335, 1982.

[29] C. A. Hall and R. W. Pitz, "A structural study of premixed hydrogen-air cellular tubular flames," *Proceedings of the Combustion Institute*, vol. 34, no. 1, pp. 973-980, 2013.

[30] S. W. Shopoff, *Combustion instabilities in non-premixed opposed-flow tubular flames. M.S. Thesis*, Nashville: Vanderbilt University, 2010.

[31] J. Kojima J and Q. V. Nguyen, "Laser pulse-stretching with multiple optical ring cavities," *Appl Opt.*, vol. 41, no. 30, pp. 6360-70., 2002.

[32] R. J. Osborne, P. A. Skaggs and R. W. Pitz, "Multi-camera/spectrometer design for instantaneous line Rayleigh/Raman/LIPF measurements in methane/air flames," in *34th Aerospace Sciences Meeting & Exhibit*, Reno, 1996.

[33] D. Goodwin, "Cantera: an object-oriented software toolkit for chemical kinetics, thermodynamics, and transport processes," Version 2.2.0 2015. [Online]. Available: http://www.cantera.org.

[34] J. Bergthorson, S. Salusbury and P. Dimotakis, "Experiments and modelling of premixed laminar stagnation flame hydrodynamics," *Journal of Fluid Mechanics,* vol. 681, pp. 340-69, 2011.

[35] B. Sarnacki, G. Esposito, R. Krauss and H. Chelliah, "Extinction limits and associated uncertainties of nonpremixed counterflow flames of methane, ethylene, propylene and n-butane in air," *Combustion and Flame,* vol. 159, pp. 1026-43, 2012.

[36] U. Niemann, K. Seshadri and F. Williams, "Accuracies of laminar counterflow flame experiments," *Combustion and Flame,* vol. 162, pp. 1540-1549, 2015.

[37] H. Kobayashia and M. Kitanoa, "Flow fields and extinction of stretched cylindrical premixed flames," *Combustion and Science Technology,* vol. 75, no. 4-6, pp. 227-239, 1991.

[38] H. K. Chelliah, C. K. Law and T. Ueda, "An experimental and theoretical investigation of the dilution, pressure and flow-field effects on the extinction condition of methane-air-nitrogen diffusion flames," *Symposium (International) on Combustion,* vol. 23, no. 1, pp. 503-511, 1991.

[39] H. Shengteng and R. W. Pitz, "Structural study of non-premixed tubular hydrocarbon flames," *Combustion and Flame,* vol. 156, no. 1, p. 51–61, 2009.

[40] C. A. Hall, W. D. Kulatilaka, N. Jiang, J. R. Gord and R. W. Pitz, "Minor species structure of premixed cellular tubular flames," *Proceedings of the Combustion Institute,,* vol. 35, pp. 1107-1114, 2015.